Dynamic BTB-domain filaments promote clustering of ZBTB proteins

Lucija Mance, Nicolas Bigot, Edison Zhamungui Sánchez, Franck Coste, Natalia Martín-González, Siham Zentout, Marin Biliškov, Zofia Pukalo, Aanchal Mishra, Catherine Chapuis, et al.

Dynamic BTB-domain filaments promote clustering of ZBTB proteins

Lucija Mance[1], Nicolas Bigot[2], Edison Zhamungui Sánchez[1], Franck Coste[1,✉], Natalia Martín-González[3,4], Siham Zentout[2], Marin Biliškov[1], Zofia Pukało[1], Aanchal Mishra[1], Catherine Chapuis[2], Ana-Andreea Arteni[5], Axelle Lateur[1], Stéphane Goffinont[1], Virginie Gaudon[1], Ibtissam Talhaoui[1], Ignacio Casuso[3], Martine Beaufour[1], Norbert Garnier[1], Franck Artzner[6], Martine Cadene[1], Sébastien Huet[2,7], Bertrand Castaing[1], Marcin Józef Suskiewicz[1,8,✉]

[1] Centre de Biophysique Moléculaire (CBM), UPR 4301, CNRS, affiliated with Université d'Orléans, 45071 Orléans Cedex 2, France

[2] Université Rennes, CNRS, IGDR (Institut de Génétique et Développement de Rennes) - UMR 6290, BIOSIT – UAR3480, 35000 Rennes, France

[3] Aix-Marseille Université, INSERM, DyNaMo, Turing centre for living systems (CENTURI), 13288 Marseille Cedex 09, France

[4] Aix-Marseille Université, CNRS, AFMB UMR 7257, 13288 Marseille Cedex 09, France

[5] Université Paris-Saclay, CEA, CNRS, Institute for Integrative Biology of the Cell (I2BC), Cryo-electron Microscopy Facility, CRYOEM-Gif, 91198 Gif-sur-Yvette, France

[6] Université Rennes, CNRS, IPR (Institut de Physique de Rennes) - UMR 6251, 35000 Rennes, France

[7] Institut Universitaire de France, 75005 Paris, France

[8] Lead contact

✉ Correspondence: marcin.suskiewicz@cnrs-orleans.fr, franck.coste@cnrs-orleans.fr

Summary

The formation of dynamic protein filaments contributes to various biological functions by clustering individual molecules together and enhancing their binding to ligands. We report such a propensity for the BTB domains of certain proteins from the ZBTB family, a large eukaryotic transcription factor family implicated in differentiation and cancer. Working with *Xenopus laevis* and human proteins, we solved crystal structures of filaments formed by dimers of BTB domains of ZBTB8A and ZBTB18 and demonstrated concentration-dependent higher-order assemblies of these dimers in solution. In cells, the BTB-domain filamentation supports clustering of full-length human ZBTB8A and ZBTB18 into dynamic nuclear foci and contributes to the ZBTB18-mediated repression of a reporter gene. The BTB domains of up to 21 human ZBTB-family members and two related proteins, NACC1 and NACC2, are predicted to behave in the same manner. Our results suggest that filamentation is a more common feature of transcription factors than currently appreciated.

Keywords: protein filaments, protein polymerisation, nuclear foci, transcription factors, gene repression, ZBTB proteins, ZBTB8A, ZBTB18, ZBTB26, NACC1

Introduction

The ZBTB (zinc finger and BTB domain-containing) family, comprising ~50 members, is among the largest transcription factor families in humans[1,2]. ZBTB proteins function primarily as transcriptional repressors, particularly in the context of differentiation and development, and have been implicated in cancer and other diseases[3–6]. The best-studied member is arguably ZBTB27 (better known as BCL6, for B cell lymphoma 6), an important factor in both normal and malignant haematopoiesis[7].

The two ZBTB proteins that we focus on here, ZBTB8A (also known as BTB/POZ and Zinc finger domains Factor on chromosome 1 or BOZF1) and ZBTB18 (also called 58 kDa Repressor Protein (RP58) or Zinc Finger-containing protein 238 (ZNF238)), also function as repressors[8,9]. More is known about ZBTB18, which plays an essential role in neuronal differentiation, brain expansion, and cognitive function according to cellular and mouse models[10–14]. Mutations in ZBTB18 have been implicated in a neurodevelopmental syndrome in humans[15–18]. Moreover, the loss of ZBTB18 through silencing is emerging as a factor in cancer development and metastasis[19–22].

Structurally, the ZBTB-family members are defined by the presence of a single Broad-complex, Tramtrack and Bric-à-brac (BTB) domain[1,23–25] at the N terminus and multiple copies of a zinc finger (ZF) domain towards the C terminus[2,4,6]. The primary role of ZF domains is to bind to specific DNA sequences, whereas the BTB domain, also known as the POx-virus and Zinc-finger (POZ) domain, mediates homodimerisation and interactions with corepressors[26,27]. The intrinsically disordered linker region between BTB and ZF domains contains potential sites of posttranslational modifications (PTMs), especially SUMOylation, which might contribute to gene repression[28–33].

Beyond homodimerisation, the BTB domains of ZBTB proteins have also been postulated as drivers of higher-order homotypic assemblies. This phenomenon is best established in the fruit-fly transcription factor GAGA and related ZBTB proteins from arthropods, whose BTB homodimers further oligomerise into hexamers (trimers of dimers)[34], which is necessary for stable chromosomal localisation of full-length proteins[35–37]. In contrast, it is unclear if BTB domains of human and other vertebrate ZBTB proteins can mediate higher-order assemblies. The BTB domain of ZBTB17 forms putative tetramers (dimers of dimers) in the crystal, but the tetramerisation is weak in solution[38]. Similarly, the higher-order assemblies of dimers that have been suggested, based on crystal contacts, for BTB domains of ZBTB16 (also known as Promyelocytic Leukemia Zinc Finger or PLZF) and ZBTB27, have not been conclusively demonstrated in solution so far[26,39–41].

The current study originated from our interest in ZBTB proteins as SUMOylation substrates. During the recombinant preparation of fragments of ZBTB8A, we serendipitously discovered that its BTB domain makes dynamic homotypic filaments. Our study adds BTB to a short list of known protein domains with this property[42,43] and explores the structural basis and functional significance of BTB-domain filamentation.

Results

The crystal of the BTB domain of ZBTB8A reveals interconnected dimers

We began with the BTB domain from human ZBTB8A (*Hs*ZBTB8A^{BTB}), which we attempted to recombinantly produce in *Escherichia coli*. However, after difficulties caused by its low solubility, we moved to the BTB domain of ZBTB8A from the frog *Xenopus laevis* (*Xl*ZBTB8A^{BTB}, 75% identical to *Hs*ZBTB8A^{BTB}) (**Figure 1A**), for which we obtained a larger amount of soluble protein. During the preparative size exclusion chromatography (SEC), *Xl*ZBTB8A^{BTB} eluted close to the void volume **(Figure 1B)**, indicating either aggregation or oligo-/polymerisation. Nevertheless, the protein was purified and crystallised.

The crystal structure of *Xl*ZBTB8A^{BTB} at 3.10 Å was solved in the *P4$_1$32* space group (**Table 1**). In each asymmetric unit, there is a single dimer with a non-crystallographic 2-fold rotational (C_2) symmetry **(Figure 1C**, *left***)**, formed in the same manner as previously observed for other ZBTB proteins[39] (*right*).

Interestingly, the *Xl*ZBTB8A^{BTB} dimer is connected on either side to a dimer from a neighbouring asymmetric unit through an extensive interdimer interaction **(Figure 1D)**. The interdimer interface has an area of ~630 Å^2 and a solvation free energy gain of −15.9 kcal/mol, within the range for probable biologically-relevant interactions.

Conservation and AlphaFold2 modelling of the interdimer interaction

The interdimer interaction observed in the *Xl*ZBTB8A^{BTB} crystals shows a C_2 symmetry, involving an equivalent surface on the two interacting subunits (**Figure 1D**). Mapping sequence conservation onto the structure revealed high sequence conservation of this surface among ZBTB8A orthologues from various species (**Figure 1E**, *main*), rivalling that of the interface needed for dimer formation (*inset*).

Next, we attempted to predict intra- and interdimer interactions using AlphaFold2 Multimer 3, accessed *via* ColabFold[44–46]. The Protein Data Bank (PDB) dataset used for training AlphaFold2 did not include our crystal structures. Five out of five models of *Xl*ZBTB8A^{BTB} tetramers showed a dimer-of-dimers assembly highly similar to that observed in our structure, with a root-mean-square deviation (RMSD) of 1.3 Å over 391 C_α atoms (**Figure 1F**). The only major difference concerned a short β-sheet in our structure (contact 2), which adopts a low-confidence α-helical conformation in the AlphaFold2 model. The interface predicted template modelling (ipTM) score of the best model reached 0.74, indicating a possible real-world interaction.

BTB dimers assemble into a helical filament in the crystal and solution

In the crystal lattice, the interdimer interactions link individual *Xl*ZBTB8A^{BTB} dimers into a right-handed helical filament with a pitch of ~15 nm and a radius of ~4 nm (**Figure 1G,H**).

To experimentally verify if a similar structure can be observed in solution, we used SEC coupled with small-angle X-ray scattering (SAXS). The SAXS data show a strong upturn for low scattering vector values indicative of large molecules and a series of three scattering events (“humps”) in harmonic positions around 0.055, 0.110, and 0.165 Å^{-1} (**Figure 1I**, *main*). These humps likely correspond to layer lines expected in a theoretical X-ray scattering pattern of a helical assembly (*inset*). We fitted the data with a helical model, achieving a good

agreement with a pitch of 15.3 nm and a radius of 3.9 nm. These parameters closely match those of our crystal filament (**Figure 1H**), indicating that *Xl*ZBTB8A^{BTB} makes similar structures in solution.

Structural elements needed for higher-order assembly

Looking closely at the evolutionarily conserved (**Figure 1E**) interdimer interface, we can distinguish two parts, contact 1 and contact 2 (**Figure 2A**).

Contact 1 is predominantly hydrophobic and involves two neighbouring α-helices (lined by the sidechains of I96, M99, S100, S103, Y104, Q106, I111, and I118) that interact with their own copies from the neighbouring BTB subunit, forming an irregular four-helix bundle (**Figure 2A**, *bottom* and **Figure S1)**. Beneath the helical bundle, M51 reaches out towards its symmetry mate, making a potential additional connection.

Contact 2, in turn, involves the residues L122, D123, and I124 (the 'LDI motif'), which represent the most C-terminal part of *Xl*ZBTB8A^{BTB} visible in the electron density (**Figure 2A**, *top*). This region also interacts with a copy of itself from the neighbouring subunit but primarily through main-chain interactions, forming a short two-stranded β-sheet. L122 and I124 might promote the β-strand conformation, as isoleucine and, to a lesser extent, leucine are strand-promoting amino acids[47].

Interdimer interface residues probed through solution experiments

To experimentally test the contribution of contacts 1 and 2 to the higher-order assembly of *Xl*ZBTB8A^{BTB}, we generated a range of mutants and compared them to the WT protein using three setups: SEC coupled with right- and low-angle light scattering (SEC-RALS/LALS) (**Figure 2B**,**H**); SEC combined with sodium dodecyl sulphate polyacrylamide gel electrophoresis (SDS-PAGE) (**Figure 2C**,**I**); and bis(sulfosuccinimidyl)suberate (BS3) crosslinking followed by SDS-PAGE (**Figure 2D**,**J**).

For WT *Xl*ZBTB8A^{BTB}, the SEC experiments reproduced the early elution seen in the preparative SEC (**Figure 2B**, **C**). The apparent molecular weight (MW) in the highest part of the peak revealed oligomers built of several dimers (**Figure 2B**). In agreement with the expected topology, BS3 crosslinking of the WT domain generated two distinct dimeric bands, possibly corresponding to the intra- and interdimer interaction, as well as a ladder of higher bands (**Figure 2D**).

Next, we tested four *Xl*ZBTB8A^{BTB} mutants carrying the following substitutions: M51R (the lower part of contact 1), I96D (contact 1), L122A/D123A/I124A or 'LDI' (contact 2), and M51R/I96D/S103R/L122A/D123A/I124A or 'Multi' (contact 1 and contact 2). Compared to WT *Xl*ZBTB8A^{BTB}, all analysed mutants showed signs of decreased or abolished higher-order assembly including a delayed SEC elution (**Figure 2B**, **C**), lower apparent MW (**Figure 2B**), and – for the strongly impaired mutants I96D and Multi – an altered crosslinking pattern with an apparent single dimeric band possibly representing the intradimer interaction (**Figure 2D**).

Preventing higher-order assembly by varying the size of residue 103

Next, we directed our focus to the narrowest point of contact 1 occupied by S103 (**Figure 2E**). We reasoned that a more voluminous sidechain (**Figure 2F**) in this position should be

incompatible with the two BTB dimers coming together, providing an elegant way of disrupting the filaments.

The crystal structures of three S103-mutated *Xl*ZBTB8A^{BTB} domains (**Table 1**) are consistent with this hypothesis **(Figure 2G**). While the S103A mutant reproduced the crystal form of the WT protein featuring the familiar filament, the S103D and S103R mutants crystallised differently from the WT protein and from each other, failing to establish the interdimer interactions needed for filamentation (**Figure 2G**).

In line with these observations, we saw only a minor impairment of the solution higher-order assembly for the S103A, but a dramatic one for the S103D and S103R mutants (**Figure 2H-J**). Among other techniques, we analysed the S103R mutant using the SEC-SAXS approach previously applied to the WT domain (**Figure 1I**). The mutant showed a SAXS curve indicative of a relatively globular protein, suggesting the loss of the large helical assemblies (**Figure 2K**).

Overall, the data from this and the previous section support the assembly of WT *Xl*ZBTB8A^{BTB} into filaments and validate the importance of contact 1 and contact 2 for this process. Based on our results, and especially the crystallisation of the S103D and S103R mutants in filament-free forms, we believe that these two mutants, as well as Multi (which includes S103R), might be completely devoid of the filamentation propensity. If this is the case, the potential signs of species larger than dimers observed for these mutants (a small peak preceding the dimeric peak in **Figure 2B,C,H,I** and a faint higher band in **Figure 2D,J**) might indicate a, likely weak/transient, interaction between dimers distinct from the one needed for filamentation.

When producing the mutants, we observed improved solubility and yields compared to WT. This indicates that the filamentous state is not necessary for stability and might in fact lower solubility and/or increase aggregation.

Concentration-dependent oligo-/polymerisation probed with SEC-RALS/LALS

Next, we performed a series of SEC-RALS/LALS analyses of WT and S103R *Xl*ZBTB8A^{BTB} at various concentrations (**Figure 3A**). The effective concentrations at elution were likely >10-fold lower than the indicated starting concentrations.

While the S103R mutant eluted at the same volume regardless of the starting concentration, the WT protein eluted progressively early with increasing starting concentration (**Figure 3A**). The average MW in the centre of the WT peak also increased with concentration, reaching, for 600 µM, a value corresponding to up to a dozen dimers (**Figure 3A**, *main*). Only at the lowest analysed starting concentrations, the elution volume of the WT protein approached that of the dimeric S103R mutant (**Figure 3A**, *inset*), suggesting a dissociation constant (K_D) of the interdimer interaction in a low micromolar or high nanomolar range. The fact that the WT samples that were analysed within minutes after dilution displayed different oligomer distributions depending on concentration means that the BTB filaments can dissociate within this time scale. In contrast, the behaviour of the S103R mutant indicates that the *Xl*ZBTB8A^{BTB} dimer has a much higher affinity and/or kinetic stability.

The observed concentration-dependent behaviour is similar to that of protein domains undergoing dynamic 'head-to-tail polymerisation'[42], but the BTB filaments do not have head-to-tail topology. Below, we refer to it as 'dynamic filamentation'.

Biophysical insights into BTB filaments at low micromolar concentrations

Subsequently, we applied three methods compatible with low micromolar concentrations including NALIM (NAtive LIquid MALDI)[48] native mass spectrometry (nMS) (**Figure 3B**), negative-stain electron microscopy (EM) (**Figure 3C-D**), and high-speed atomic-force microscopy (HS-AFM) (**Figure 3E-G**).

NALIM uses matrix-assisted laser desorption-ionisation (MALDI) to transfer a protein from a liquid deposit into the gas phase under non-denaturing conditions. Importantly, the likelihood of a native interaction remaining intact in NALIM does not necessarily directly correlate with its stability in solution. One reason for this is that, as the protein leaves the aqueous solvent, the hydrophobic effect ceases to operate, while existing ionic interactions become reinforced. Moreover, gas-phase dissociation is an irreversible process that bears no relation to an equilibrium affinity. The analysis was performed at 2.5 µM, a concentration low enough to minimise the risk of nonspecific gas-phase aggregation. We observed a range of oligomers of *Xl*ZBTB8A^{BTB} WT, with an octamer as the largest detectable species (**Figure 3B**, *top*). The absence of oligomers above a trimer in the S103R mutant (*bottom*) suggests that the observed larger WT oligomers can be attributed primarily to specific self-association. Considering our other data, the peaks corresponding to odd subunit numbers in both samples almost certainly result from partial gas-phase dissociation of even-numbered complexes. The S103R trimer peak might reflect a transient association between dimers of this mutant in solution that we speculated about when interpreting SEC and crosslinking results. Given these qualifications, the NALIM results demonstrate, in a more direct way than solution techniques with a lower mass resolution do, the formation of species composed of multiple copies of the WT *Xl*ZBTB8A^{BTB} domain.

We next analysed WT and S103R *Xl*ZBTB8A^{BTB} with negative-stain EM. The protein was analysed at a concentration of 1.1 µM, which might have increased during drying. For the WT protein, we observed numerous noodle-shaped particles consistent with filaments (**Figure 3C**, *left*), which were particularly visible in darker grid regions (*right*). In contrast, the S103R mutant showed only small particles difficult to distinguish from the background (**Figure 3D**).

Lastly, we analysed WT *Xl*ZBTB8A^{BTB} using HS-AFM by adsorbing the protein, diluted to 3 µM, onto mica. The imaging revealed particles with a range of sizes, from potential dimers to polymers (**Figure 3E**). The average height of 7.4 ± 1.1 nm (**Figure 3F**) matches well the diameter of the crystal filament (~8 nm, **Figure 1H**). A closer look at individual assemblies reveals apparent helical structures in reasonable agreement with the crystal filament (**Figure 3G**), with the slight disparities in pitch coming either from inherent flexibility or from the dilation tip effect in the XY direction.

The results obtained with these three techniques support the self-assembly of *Xl*ZBTB8A^{BTB} into helical filaments already within the low micromolar regime.

Filamentation propensity is conserved in ZBTB8A and related paralogues

We next revisited bacterial production of the BTB domain of *Hs*ZBTB8A^{BTB}. As the S103 residue is conserved between the frog and human proteins, we created the S103R mutant of *Hs*ZBTB8A^{BTB} to compare it to the WT form. The results of the SEC-RALS/LALS analysis of a single starting concentration of each protein (**Figure 3H**) were qualitatively similar to those for *Xl*ZBTB8A^{BTB} (**Figure 2H,3A**).

To investigate whether other members of the ZBTB family also form BTB-domain filaments, we first bioinformatically examined its closest paralogues: ZBTB8B, ZBTB10, and ZBTB46 (the 8A-8B-46-10 subclade), observing a high conservation of contact 1 and 2 residues (**Figure 4A**). Furthermore, we created AlphaFold2 models of BTB-domain tetramers. For each of these proteins, five out of five models showed an interdimer arrangement similar to that seen in *Xl*ZBTB8A^{BTB} crystals (**Figure 4A**). Together, these analyses suggest the conservation of filamentation in this subclade.

Family-wide prediction of BTB filamentation among ZBTB proteins

We next analysed the conservation of residues needed for ZBTB8A-like filaments in a broader subset of human ZBTB proteins (**Figure 4B**). For some of the selected proteins (ZBTB18, ZBTB44, ZBTB6, ZBTB43), we did not have prior indications whether their BTB domains do or do not form ZBTB8A-like filaments; however, we included also a few proteins whose BTB domains are well-characterised and do not form ZBTB8A-like filaments in crystals (ZBTB7A, ZBTB16, ZBTB27)[39,40,49].

While contact 2 residues appeared limited to ZBTB8A, contact 1 residues were more widely conserved (**Figure 4B**), and we hypothesised that BTB domains of some ZBTB proteins might be able to form filaments through contact 1 alone. Based on our analysis of *Xl*ZBTB8A^{BTB} (**Figure 2G-K**), contact 1 interaction requires a serine or another small amino acid in position 103 (ZBTB8A numbering) (**Figure 4C**). Among the proteins analysed in **Figure 4B**, this serine is replaced by more voluminous amino acids specifically in the three proteins known not to form ZBTB8A-like BTB filaments, suggesting this residue as a potential evolutionary ‘marker’ of filamentation.

With this in mind, we performed a phylogenetic analysis of all 49 canonical human members of the ZBTB family (**Figure 4D**). While the obtained phylogenetic tree was not fully robust, ZBTB proteins were generally reproducibly grouped into clades broadly consistent with previously published trees[2,50]. Analysing their sequences, we observed that a serine in position 103 is present in proteins from three clades that we termed I, II, and III (**Figure 4D**). On the other hand, the majority of ZBTB proteins outside these clades contain a more voluminous residue in this position. The latter group includes all ZBTB proteins whose BTB domains had been crystallised before, and, fittingly, none of these crystal structures features contacts consistent with ZBTB8A-like filaments.

We also performed large-scale AlphaFold2 modelling of BTB tetramers. The BTB domains of most ZBTB proteins from clades I, II, and III were predicted to form dimers-of-dimers consistent with *Xl*ZBTB8A^{BTB}-like filaments in at least one out of five models (**Figure 4D**). In contrast, BTB domains of ZBTB proteins outside the three mentioned clades, with a few exceptions, were not predicted to assemble into such structures.

The presence of a serine in position 103 and the results of AlphaFold2 modelling provide two largely independent criteria for predicting a propensity to form ZBTB8A-like BTB filaments, so it is reassuring that they converge on similar proteins. However, both these criteria have limitations. As AlphaFold2 is informed by a multiple-sequence alignment[45], its results will be influenced by the extent to which the properties of the target BTB domain are shared by homologous sequences automatically included in the alignment. Similarly, a serine in position 103 is not an unequivocal indicator of ZBTB8A-like filamentation, because the BTB interdimer

interface requires multiple residues, and, while the small volume of S103 is important in ZBTB8A, it might be less important in hypothetical cases where the interacting helices are shifted. We prefer to focus on clades rather than individual proteins, because the formation of filaments with this particular form is more likely to be inherited from a common ancestor than to emerge in isolated cases. Therefore, we conclude that ZBTB proteins from clades I, II, and III are candidates for ZBTB8A-like BTB-domain filamentation.

Oligo-/polymerisation of BTB domains of ZBTB18 and ZBTB26

In order to experimentally examine this hypothesis, we recombinantly produced BTB domains of selected ZBTB proteins from these clades, including ZBTB18, ZBTB5, ZBTB26, ZBTB12, ZBTB20, and ZBTB43. We succeeded in purifying only the BTB domains of ZBTB18 (*Hs*ZBTB18^{BTB}, **Figure 5A**) and ZBTB26 (*Hs*ZBTB26^{BTB}), as the other domains were exclusively insoluble.

While we failed to crystallise *Hs*ZBTB26^{BTB}, we obtained crystals of *Hs*ZBTB18^{BTB} and solved its structure in the $I4_1$ space group at 4.15 Å (**Table 1**). The structure contains eight BTB molecules in the asymmetric unit, which belong to two similar tetramers (dimers-of-dimers). Each tetramer further extends by interacting with tetramers from neighbouring units, forming a helical filament highly similar to that for *Xl*ZBTB8A^{BTB} (**Figure 5B**,**C**).

A closer comparison of the *Hs*ZBTB18^{BTB} and *Xl*ZBTB8A^{BTB} interdimer interactions shows that the small β-sheet seen for *Xl*ZBTB8A^{BTB} (contact 2) is absent in *Hs*ZBTB18^{BTB} (**Figure 5D**). The interdimer interaction is thus limited to contact 1, which is very similar to that for *Xl*ZBTB8A^{BTB}. Of note, the interdimer interaction observed in the *Hs*ZBTB18^{BTB} structure is almost identical to that proposed for this protein by AlphaFold2, with an RMSD of 1.4 Å over 395 Cα atoms (**Figure 5E**).

A series of SEC-RALS/LALS analyses of *Hs*ZBTB18^{BTB} at different concentrations (**Figure 5F**) gave qualitatively very similar results to an equivalent experiment performed for *Xl*ZBTB8A^{BTB} (**Figure 3A**), consistent with concentration-dependent higher-order assemblies of stable dimers. WT *Hs*ZBTB26^{BTB} – for which we analysed only one starting concentration – showed early elution and high apparent MW indicative of a large assembly (**Figure 5G**). For both *Hs*ZBTB18^{BTB} and *Hs*ZBTB26^{BTB}, the higher-order assembly was strongly impaired upon substituting the serine equivalent to S103 of ZBTB8A with arginine (S102R for ZBTB18 and S108R for ZBTB26, **Figure 5F,G**), suggesting a ZBTB8A-like filament topology.

These results indicate that the ZBTB8A-like higher-order assembly of BTB dimers is a feature of at least three proteins: ZBTB8A, ZBTB18, and ZBTB26, which span clades I, II, and III (**Figure 4D**). The solubility issues observed with BTB domains of some other members of these clades might also reflect filamentation, but this needs to be confirmed.

Filaments of the BTB domain of NACC1 suggested by its crystal structure

As BTB domains are present in many human proteins outside the ZBTB family, we wondered if any of them might be closely related to BTB domains of ZBTB proteins from clades I, II, and III and also exhibit filament formation. A series of Basic Local Alignment Search Tool (BLAST)[51] searches identified BTB domains of NACC1 and NACC2 as closely related to the clade-III protein ZBTB37.

NACC1 (for Nucleus ACCumbens associated 1) consists of an N-terminal BTB domain and a C-terminal DNA-binding BEN domain (named after BANP, E5R, and NACC1) (**Figure 5H**). While the BTB domain of NACC1 (*Hs*NACC1^{BTB}) has been crystallised[52], it has not been reported to form higher-order assemblies in solution. However, initial insolubility was reported, which was overcome by mutating a surface aromatic residue (F98D)[52]. Interestingly, this mutation is the exact equivalent of the filament-deficient I96D substitution in *Xl*ZBTB8A^{BTB} (**Figure 2B-D**). The F96D mutation likely resulted in the domain behaving like a dimer, discouraging the authors from analysing higher-order crystal contacts. Revisiting this crystal structure, we observed a similar filamentous arrangement to that in our *Xl*ZBTB8A^{BTB} and *Hs*ZBTB18^{BTB} structures (**Figure 5I**). The angle between interacting *Hs*NACC1^{BTB} dimers is altered compared to that for *Xl*ZBTB8A^{BTB}, possibly due to a glycine in the position equivalent to S103 of ZBTB8A allowing a closer contact-1 interaction (**Figure 5J**).

These observations suggest that the BTB domains of NACC1 and likely its paralogue, NACC2, can form ZBTB8A-like filaments, which should be tested in solution.

Filamentation-dependent localisation of ZBTB8A and ZBTB18 to nuclear foci

The formation of dynamic protein filaments is an established mechanism whereby multiple copies of a protein cluster together in specific cellular locales[42,53–55]. To test if BTB-domain filamentation determines the cellular localisation of full-length ZBTB proteins, we transiently overexpressed mCherry-tagged human ZBTB8A (*Hs*ZBTB8A-mCherry) or ZBTB18 (*Hs*ZBTB18-mCherry) (**Figure 6A**) in U2OS cells.

Within the nucleus, the WT forms of both proteins distribute between two populations: one diffusive, spread across the nucleoplasm, and another that accumulates within discrete foci (**Figure 6B,C**). *Hs*ZBTB8A-mCherry displays a stronger tendency to form foci compared to *Hs*ZBTB18-mCherry. A similar punctate nuclear localisation has previously been reported for endogenous ZBTB8A and ZBTB18[56].

In contrast to the *Hs*ZBTB18-mCherry foci, which are evenly distributed throughout the nucleus, the *Hs*ZBTB8A-mCherry foci appear to form preferentially at the nucleolar periphery, a site of repressive chromatin[57–59]. This was confirmed by analysing cells cotransfected with a vector expressing an enhanced green fluorescent protein (eGFP)-tagged nucleolin (**Figure 6D**). Moreover, *Hs*ZBTB8A-mCherry but not *Hs*ZBTB18-mCherry appears to colocalise with promyelocytic leukaemia (PML) bodies – structures linked to protein SUMOylation and gene repression[60] – visualised by the coexpression of eGFP-tagged PML isoform 4 (**Figure 6D**).

In the same experiment, we monitored the subcellular localisation of various mutants of the two ZBTB proteins, observing a good agreement between the loss of punctate nuclear distribution (**Figure 6B,C**) and the impaired interdimer interactions observed above in the isolated BTB domain *in vitro* (**Figure 2B-D,G-J** and **5F**). A discrepancy with *in-vitro* results was observed only for the LDI mutation of ZBTB8A, which caused only a partial decrease in filament formation in an isolated BTB domain *in vitro* (**Figure 2B,C,D**) but led to the complete loss of nuclear foci and a partial delocalisation to the cytoplasm in the full-length protein in the cell (**Figure 6B**). This might indicate that, in addition to stabilising the BTB interdimer contacts, the LDI motif – while unlikely to be part of a nuclear localisation signal (NLS) – might contribute to nuclear retainment. Nonetheless, all these results strongly suggest that the

formation of dynamic BTB-domain filaments is required for, and likely is the driver of, the clustering of ZBTB8A and ZBTB18 into distinct nuclear foci.

Nuclear foci of ZBTB8A and ZBTB18 show slow exchange

For WT *Hs*ZBTB8A-mCherry, analysing the turnover within foci using fluorescence recovery after photobleaching (FRAP) revealed a slow exchange, with only ~20% of the bleached fluorescence recovering after 7 s (**Figure 6E,F**). Upon the S103R mutation, this behaviour gave way to a uniquely diffusive population undergoing a very fast exchange (100% within 1 or 2 s). A very similar fast exchange was observed for the S102R mutant of *Hs*ZBTB18-mCherry, compared to which the WT *Hs*ZBTB18-mCherry molecules both within (~80% recovery within 7s) and outside (100% within 6 s) foci appeared slowed down – indicating oligo- or polymerisation of both these WT *Hs*ZBTB18-mCherry populations (**Figure 6G,H**).

These results demonstrate that, as observed for other foci driven by dynamic filamentation[42,43,53], the molecules within ZBTB foci undergo a measurable exchange with the surrounding molecules. The turnover of the molecules in the foci, however, is slowed down compared to diffusive molecules, particularly in the case of ZBTB8A. This likely reflects the constraining effect of the BTB interdimer interactions, potentially compounded by a further filament-dependent event, such as tangling of the ZBTB filaments with each other or enhanced binding between ZBTB filaments and DNA.

ZBTB18 filamentation contributes to the repression of a reporter gene

We next evaluated the impact of the impairment of the BTB-domain filamentation on the transcriptional repressor function of ZBTB18[9,18,21,22,61], which is better defined than that of ZBTB8A. For this, we used a luciferase reporter assay with a plasmid containing a firefly luciferase gene preceded by ten ZBTB18-binding DNA motifs ('BS10')[9,18,61] (**Figure 7A**). The data were normalised using a cotransfected renilla luciferase reporter plasmid lacking the BS10 sequence.

Using this setup, we reproduced specific repression of firefly luciferase when additionally cotransfecting COS-7 cells with a plasmid encoding untagged WT ZBTB18 (**Figure 7B**). The effect depended on the amount of the ZBTB18 vector used and was abolished upon the charge-reversal mutations of ZBTB18 residues predicted to interact with DNA (K426E/R427E) based on the homology to ZBTB10[62]. In fact, this mutant, when overexpressed, enhanced firefly luciferase expression, plausibly indicating interference with the endogenous ZBTB18 present in these cells through the formation of mixed filaments. Importantly, the filament-deficient S102R mutant of ZBTB18 caused a diminished repression compared to WT ZBTB18, indicating a role for BTB-domain filaments in defining the full repressive potential of ZBTB18. The difference in repression between WT and S102R ZBTB18 does not appear to be due to a difference in ZBTB18 protein levels, which, for the same vector amount, are similar between variants according to immunoblotting (**Figure 7C**). The surprising migration of ZBTB18 (MW ~58 kDa) near the 75-kDa SDS-PAGE marker has been reported[63].

In addition, we performed a quantitative reverse-transcription polymerase chain reaction (RT–qPCR) experiment in U2OS cells that transiently overexpressed eGFP-tagged ZBTB18 (*Hs*ZBTB18-eGFP) in a WT or S102R form or an empty eGFP vector. While these results lack statistical significance due to variability between replicates, a possible repression of a

panel of previously reported target endogenous genes[19,21] was observed upon the overexpression of WT but not S102R ZBTB18 (**Figure S2**), providing preliminary evidence that the insights from the reporter assay may extend to endogenous targets.

Together, these results suggest that the BTB-domain filamentation contributes to the biological functioning of ZBTB proteins, which should be further explored across various ZBTB-family members.

Discussion

The BTB is a common protein domain, typically functioning as a homodimerisation module[1,23–25,39,49]. Here, we present the first conclusive demonstration of a higher-order homotypic assembly of BTB dimers into helical filaments. The filaments that we observed for ZBTB8A and ZBTB18 are structurally distinct from those previously suggested for some other ZBTB proteins based on crystal contacts[26,39–41] and from pharmacologically-induced filaments of the BTB domain of ZBTB27[64].

In terms of their properties, the observed filaments fall into the category of dynamic filaments[42], a type that has been reported for various proteins, including cellular signalling and polarity regulators[53,54,65–70], E3 ubiquitin ligase adaptors[55,71], gene silencing mediators[43,72,73], RNA-binding proteins[74,75], and a few transcription factors[76–81]. These formations are structurally similar to, but mechanistically distinct from, cytoskeletal filaments, which tend to be long and to depend on other factors and chemical energy for their assembly and disassembly. In contrast, dynamic filamentation involves spontaneous and reversible formation of relatively short, oligo- or polymeric, chains, where the average size is dictated by the local concentration[42]. These characteristics appear to be shared by the BTB domains of ZBTB8A and ZBTB18, which, after purification, spontaneously produce distributions with a varying average size in a concentration-dependent manner (**Figure 3** and **5F**). It was possible to produce mutants forming only (or mostly) individual building blocks (in this case, dimers), suggesting that filamentation is not necessary for protein stability. On the other hand, our attempts to mutate the intradimer interface (L10D/F23A/A44R) led to insolubility, possibly reflecting the obligate status of the dimeric building block, in line with its intertwined structure[39], cotranslational assembly[82,83], and previous experiments[84].

The dynamic filamentation propensity of a protein can reside in a single domain, as in the case of Sterile α Motif/Pointed (SAM/PNT), Phox and Bem1/Dishevelled-Axin (PB1/DIX), and Vernalisation/VIN3-like (VEL) domain families[42,43] or depend on multiple domains, as in the protein SPOP (speckle-type POZ protein), which dimerises with high affinity *via* a BTB domain (related to that of ZBTB proteins) and then uses other domains to form dynamic higher-order assemblies[55,71,85]. Our data indicate that, unlike in SPOP, the BTB domain of ZBTB8A is sufficient for filamentation, thus resembling SAM/PNT, DIX/PB1, or VEL domains. On the other hand, BTB-domain filaments differ from those formed by the three mentioned domain families in symmetry. In the SAM/PNT, DIX/PB1, or VEL filaments, the 'head' of each individual subunit interacts with the 'tail' of another, resulting in polar structures with two different ends[42,43,76,86] (**Figure 7D**, *top*). In contrast, our structures demonstrate that BTB domains form C_2-symmetric head-to-head dimers, and then each dimer connects with two others through a C_2-symmetric tail-to-tail interaction (**Figure 7D**, *bottom*). As a result, the BTB filaments are nonpolar, with two equivalent ends.

These considerations concerning topology and symmetry have implications for the evolution and prediction of protein filamentation. For its evolution, because C_2-symmetric interfaces are known to be abundant in nature and emerge rapidly through mutation. This is likely related to the composition of such interfaces of two equivalent halves, meaning that favourable contacts that arise by chance are doubled by symmetry[87,88]. A domain that already makes a C_2 homodimer could further evolve into a filament if 1) it develops a second C_2-symmetric homodimerisation interface at the tail, as in the BTB filaments described here, or 2) it

becomes fused with another C_2-symmetrically homodimerising domain as a result of domain shuffling, as apparently is the case for SPOP. It has recently been reported that proteins already endowed with a rotational symmetry can be transformed into a filament through a small number of surface mutations that fortuitously generate a new rotationally symmetric interface[89]. Similar evolutionary trajectories might have been common in nature.

Topology and symmetry also hold consequences for the prediction of filaments. A recent AlphaFold-based approach to the prediction of oligomeric states involves the initial modelling of a homodimer for each protein and, in the case of a high-confidence head-to-tail arrangement, a geometrical extrapolation of the homodimer to a ring or a filament[90]. This approach successfully predicts some head-to-tail filaments, but it cannot predict higher-order arrangements of dimers such as those formed by BTB domains. We show that AlphaFold modelling of tetramers can be an effective strategy for uncovering protein filaments composed of dimers. SPOP-like filaments reliant on two different domains could potentially also be predicted by searching for proteins with two known dimerisation domains using standard bioinformatics.

The results of our cellular experiments (**Figure 6**, **7A-C**, **S1**) – in which the studied proteins were overexpressed – serve as first indications that BTB domain-mediated filamentation is operational in cells and can affect the localisation and function of ZBTB proteins. However, these aspects should be further investigated at endogenous protein levels and chromosomal loci, in various cell types and at different developmental stages. At the fundamental level, based on the previously proposed mechanisms, the BTB domain-mediated clustering of ZBTB molecules could serve to 1) enhance binding to ligands (including binding motifs on chromosomal DNA) through cooperativity (if the filament assembles on the DNA, **Figure 7E**, *top left*), avidity (if it simultaneously binds to multiple sites, *top right*), or simply by promoting rebinding of a ligand to another subunit in a chain after it dissociated from a previous one[42,91,92]; 2) regulate subcellular and subnuclear localisation[42,81,93] ; and/or 3) affect the structure and topology of the bound DNA, including looping or bridging (**Figure 7E**, *bottom*)[73]. These mechanisms are generally similar to those enabled by non-filamentous oligomers with a defined subunit number (for example, λ phage repressor octamers[94,95]). However, the formation of dynamic filaments has, at least in theory, a greater regulatory potential, as it can give rise to larger assemblies[42]. It remains to be seen if the mentioned mechanisms apply to ZBTB proteins and how they manifest within a biological system. A preview of the expected complexity is offered by the convoluted history of research into the role of multimerisation in transcription factor function, including the data for Yan, a SAM domain-containing repressor from the fruit fly[77], where filamentation does not greatly affect chromosomal distribution[96] but is nonetheless functionally essential[92,93,97,98]. The role of dynamic filamentation might be similarly complex for each individual ZBTB protein, and further compounded if heterotypic filaments of different ZBTB proteins are possible. The BTB domain-mediated clustering might also contribute to the biological function indirectly, *e.g.* by impacting the SUMOylation of ZBTB proteins[31]. In turn, BTB-domain filaments could be regulated by PTMs, including the potential phosphorylation of the conserved serine located at the interdimer interface.

In addition to their physiological functions, the uncovered mechanism might explain the oncogenic potential of fusions between ZBTB10 and NACC2 proteins and protein kinases[99–101]. Indeed, BTB-domain filaments could cluster the kinase domains together to promote their *trans*-autophosphorylation and activation[102,103] (**Figure 7F**).

The identification of an overlooked filamentation tendency within a well-studied transcription factor family prompts the question if the ability to form dynamic filaments could be more frequent among human transcription factors and, more generally, proteins than is currently known. In this regard, the tendency of filament-forming proteins to be insoluble upon overexpression[42,76], with which this study began, might be one reason why further cases of dynamic protein filamentation – and their biological role – likely still await discovery.

Limitations of the study

The study combines insights from various techniques, each of which has limitations. *In-vitro* experiments were performed with isolated BTB domains. Crystal structures might not reflect predominant states in solution. Live-cell imaging and RT-qPCR were performed in transformed cells using transient overexpression of proteins tagged with large fluorescent domains. The insights from the luciferase reporter assay, which involved untagged proteins, are limited due to an overexpression approach, the use of a monkey cell line, an artificial BS10 sequence, and different chromatinisation of plasmid-embedded compared to chromosomal loci. Finally, the proposal that the observed behaviour might extend to BTB domains of numerous human proteins requires experimental validation, as do the proposed molecular mechanisms.

Acknowledgements

We thank Marc Boudvillain, Evgeniia Prokhorova, Agata Nawrotek Maalouf, and Max V. Staller for discussions. We thank Béatrice Vallée-Méheust and Hélène Bénédetti for COS7 cells, Ivan Ahel for U2OS cells, and Olivier Diaz, Christine Varon, Christelle Dussert, and Michael Kastan (*via* AddGene) for plasmids. We acknowledge the SOLEIL synchrotron and thank Pierre Legrand and Andrew Thompson for assistance at beamline PROXIMA 1 and Aurélien Thureau at beamline SWING. With regards to optical microscopy, we thank the Microscopy-Rennes Imaging Center (BIOSIT, Univ Rennes 1), a member of France-BioImaging supported by the French National Research Agency (ANR) (grant no ANR-10-INBS-04), for access and Stéphanie Dutertre and Xavier Pinson for their assistance. With regards to EM, we thank the French Infrastructure for Integrated Structural Biology (FRISBI), supported by the ANR (grant no ANR-10-INBS-0005), for access and Malika Ouldali for her assistance. We thank Guillaume Gabant and the MO2VING platform for quality-control MS and the Région Centre Val de Loire (MALDITOF, SyMBioMS grants) and the European FEDER funds (grant no 2699-33931) for supporting MS instruments. L.M. and E.Z.S. are financed by the Université d'Orléans. M.J.S. is supported by the European Research Council (Starting Grant 'SUMOwriteNread', grant no 101078837), la Ligue contre le Cancer, and the CNRS. M.J.S. is an associated fellow of Le Studium and ATIP-Avenir. For this work, S.H.'s group received financial support from the Institut Universitaire de France.

Author contributions

L. M. purified proteins, performed crosslinking, SEC, AF2 modelling, and luciferase reporter experiments and contributed to crystallisation, EM, live-cell imaging, writing, and figure design. F. C. solved structures and performed SEC-SAXS, EM, and SEC-RALS/LALS. Z. P. and A. L. assisted with protein purification, crystallisation, and phylogenetic analysis. A. M. contributed to AF2 models and writing. S. G. and V. G. provided laboratory management. I. T. performed immunoblotting and assisted with cell culture. N. G. contributed to writing. B. C. provided supervision, contributed to writing and study design. M. J. S. designed and supervised the study, purified proteins, analysed structures and phylogeny, and coordinated manuscript writing and figure design.

F. A. performed SAXS data interpretation. N. M.-G. performed, and I.C. supervised, AFM analysis. A.-A. A. assisted with EM.

E. Z. S. performed NALIM native MS, E. Z. S. and M. B. performed data interpretation for NALIM. M.C. and M.B. contributed to NALIM study design. M. C. supervised NALIM and contributed to writing and figure design.

N. B. performed RT-qPCR. S. H., S.Z., and C.C. performed cell culture and live-cell imaging. S. H. designed and supervised cellular experiments, contributed to study design, writing, and figure design.

Declaration of interests

The authors declare no competing interests.

Figures

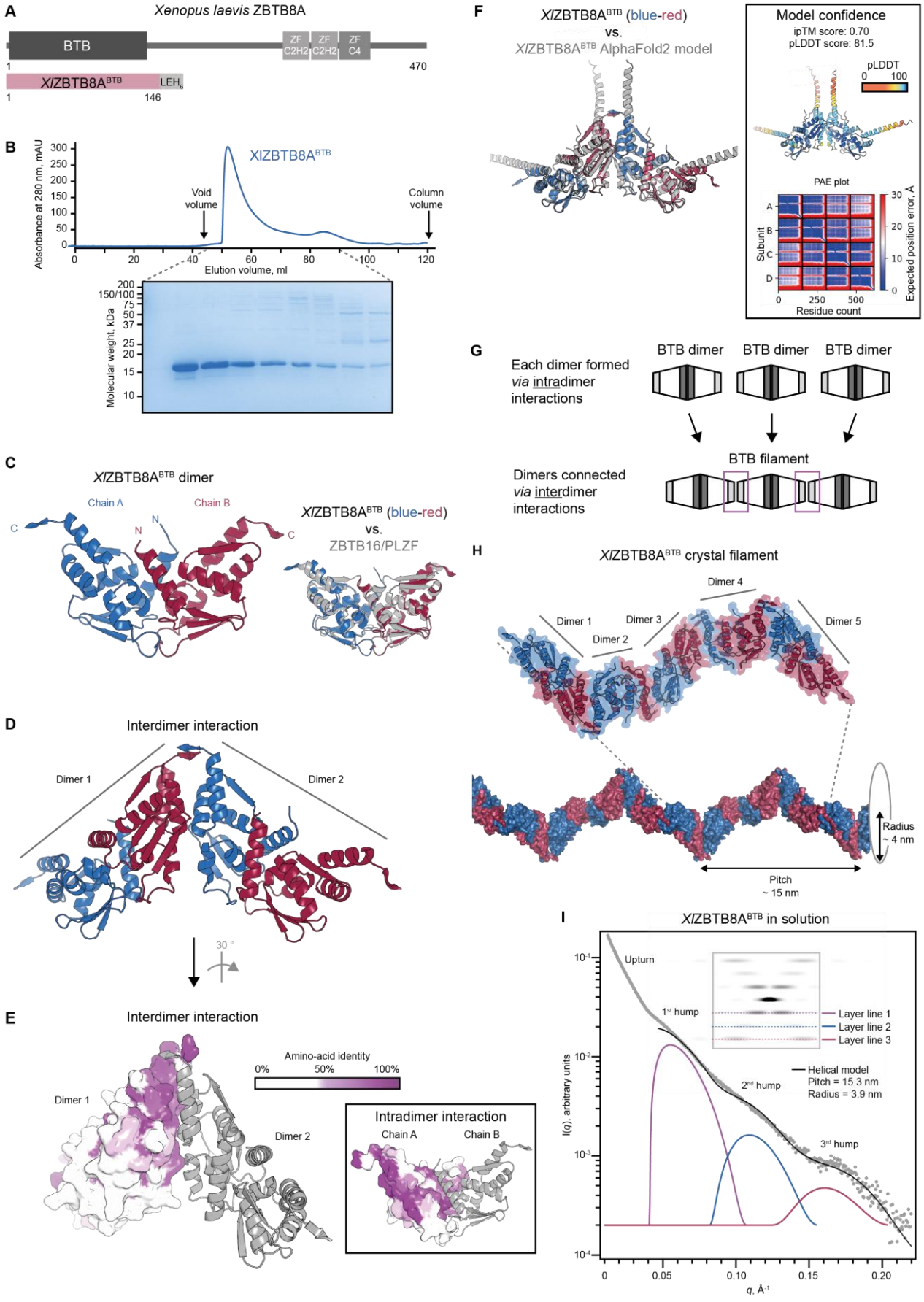
A
Xenopus laevis ZBTB8A
BTB
ZF C2H2
ZF C2H2
ZF C4
1
470
XlZBTB8A^BTB
LEH
1
146
B
XlZBTB8A^BTB
Absorbance at 280 nm, mAU
Void volume
Column volume
Elution volume, ml
Molecular weight, kDa
C
XlZBTB8A^BTB dimer
Chain A
Chain B
N
C
XlZBTB8A^BTB (blue-red)
vs.
ZBTB16/PLZF
D
Interdimer interaction
Dimer 1
Dimer 2
30 °
E
Interdimer interaction
Amino-acid identity
0%
50%
100%
Dimer 1
Dimer 2
Intradimer interaction
Chain A
Chain B
F
XlZBTB8A^BTB (blue-red)
vs.
XlZBTB8A^BTB AlphaFold2 model
Model confidence
ipTM score: 0.70
pLDDT score: 81.5
pLDDT
PAE plot
Subunit
Residue count
Expected position error, Å
G
Each dimer formed via intradimer interactions
BTB dimer
BTB dimer
BTB dimer
BTB filament
Dimers connected via interdimer interactions
H
XlZBTB8A^BTB crystal filament
Dimer 1
Dimer 2
Dimer 3
Dimer 4
Dimer 5
Radius ~ 4 nm
Pitch ~ 15 nm
I
XlZBTB8A^BTB in solution
Upturn
1st hump
2nd hump
3rd hump
Layer line 1
Layer line 2
Layer line 3
Helical model
Pitch = 15.3 nm
Radius = 3.9 nm
I(q), arbitrary units
q, Å^-1

Figure 1. Crystal structure of *Xl*ZBTB8A^{BTB} reveals a helical filament

A Domain architecture of ZBTB8A from *Xenopus laevis* and the crystallised fragment

B Preparative SEC of *Xl*ZBTB8A^{BTB}

C *Left*, crystal structure of the *Xl*ZBTB8A^{BTB} dimer. *Right*, superposition of the *Xl*ZBTB8A^{BTB} and ZBTB16/PLZF BTB (PDB: 1BUO) homodimers

D The interdimer interface

E The interdimer interface with one dimer coloured according to sequence conservation among ZBTB8A orthologues. *Inset*, the intradimer interface

F Comparison of *Xl*ZBTB8A^{BTB} interdimer assembly from crystal structure and AlphaFold2 model. *Inset*, model coloured according to confidence and the corresponding Predicted Aligned Error (PAE) plot.

G The principle of the assembly of BTB filaments

H A fragment of the crystal *Xl*ZBTB8A^{BTB} filament

I Experimental and modelled SEC-SAXS data of *Xl*ZBTB8A^{BTB} WT at the starting SEC concentration of 570 µM. The same experimental data are shown for WT in Figure 2K. A theoretical helical fibre diffraction pattern is inset. The data were deposited in SASBDB under SASDR98. The parameters of the fitted model are in Table S3.

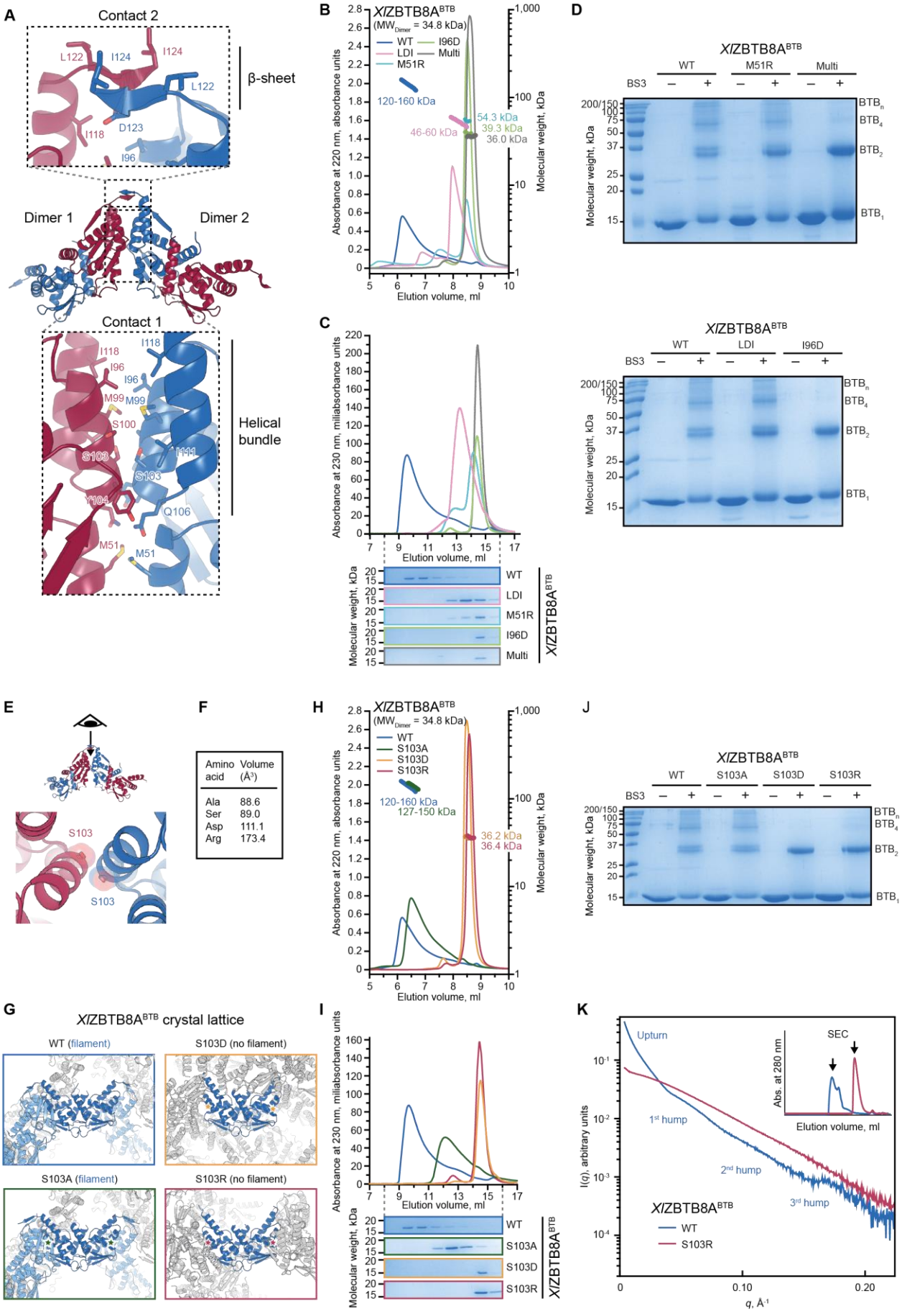
A
Contact 2
L122
I124
I124
L122
β-sheet
I118
D123
I96
Dimer 1
Dimer 2
Contact 1
I118
I118
I96
I96
M99
M99
S100
S103
I111
S103
Y104
Q106
M51
M51
Helical bundle
B
XlZBTB8ABTB
(MWDimer = 34.8 kDa)
WT
I96D
LDI
Multi
M51R
120-160 kDa
46-60 kDa
54.3 kDa
39.3 kDa
36.0 kDa
Absorbance at 220 nm, absorbance units
Molecular weight, kDa
Elution volume, ml
C
Absorbance at 230 nm, miliabsorbance units
Elution volume, ml
Molecular weight, kDa
WT
LDI
M51R
I96D
Multi
XlZBTB8ABTB
D
XlZBTB8ABTB
WT
M51R
Multi
BS3
Molecular weight, kDa
BTBn
BTB4
BTB2
BTB1
XlZBTB8ABTB
WT
LDI
I96D
BS3
Molecular weight, kDa
BTBn
BTB4
BTB2
BTB1
E
S103
S103
F
Amino acid
Volume (Å3)
Ala 88.6
Ser 89.0
Asp 111.1
Arg 173.4
H
XlZBTB8ABTB
(MWDimer = 34.8 kDa)
WT
S103A
S103D
S103R
120-160 kDa
127-150 kDa
36.2 kDa
36.4 kDa
Absorbance at 220 nm, absorbance units
Molecular weight, kDa
Elution volume, ml
J
XlZBTB8ABTB
WT
S103A
S103D
S103R
BS3
Molecular weight, kDa
BTBn
BTB4
BTB2
BTB1
G
XlZBTB8ABTB crystal lattice
WT (filament)
S103D (no filament)
S103A (filament)
S103R (no filament)
I
Absorbance at 230 nm, miliabsorbance units
Elution volume, ml
Molecular weight, kDa
WT
S103A
S103D
S103R
XlZBTB8ABTB
K
Upturn
SEC
Abs. at 280 nm
Elution volume, ml
1st hump
2nd hump
3rd hump
I(q), arbitrary units
XlZBTB8ABTB
WT
S103R
q, Å-1

Figure 2. Interdimer interface residues of *Xl*ZBTB8A^{BTB} probed through solution analysis

A Interdimer interaction interface with zoomed-in contact 1 and contact 2. An enlarged view of contact 2 is in **Figure S1**.

B SEC-RALS/LALS of *Xl*ZBTB8A^{BTB} WT and indicated mutants at the starting concentration of 300 µM. The MW of a dimer is provided. The WT data are the same as in Figure 2H. Thin lines correspond to UV traces and thick lines to apparent MW derived from light scattering.

C SEC of *Xl*ZBTB8A^{BTB} combined with SDS-PAGE at the starting concentration of 100 µM. The WT data are the same as in Figure 2I.

D SDS-PAGE analysis of BS3 crosslinking of *Xl*ZBTB8A^{BTB} WT and indicated mutants. BTB_n refers to a likely number of BTB domains in the indicated band.

E A zoomed-in view of the interdimer interaction seen from the top

F Approximate van der Waals volumes of indicated amino acids

G The packing of *Xl*ZBTB8A^{BTB} dimers in crystal structures of WT and indicated mutants. The location of the mutation is marked with a star. Crystal contacts reflecting WT-like filaments are coloured light blue.

H Like B, including the same WT data as in B with further mutants.

I Like C, including the same WT data as in C with further mutants.

J Like D, but with further mutants.

K Experimental SAXS data of *Xl*ZBTB8A^{BTB} WT and S103R at the starting SEC concentration of 570 µM. The same WT data are in Figure 1I. SEC chromatograms are shown in the inset, with arrows indicating fractions analysed with SAXS. The data were deposited in SASBDB under SASDR98 and SASDRA8.

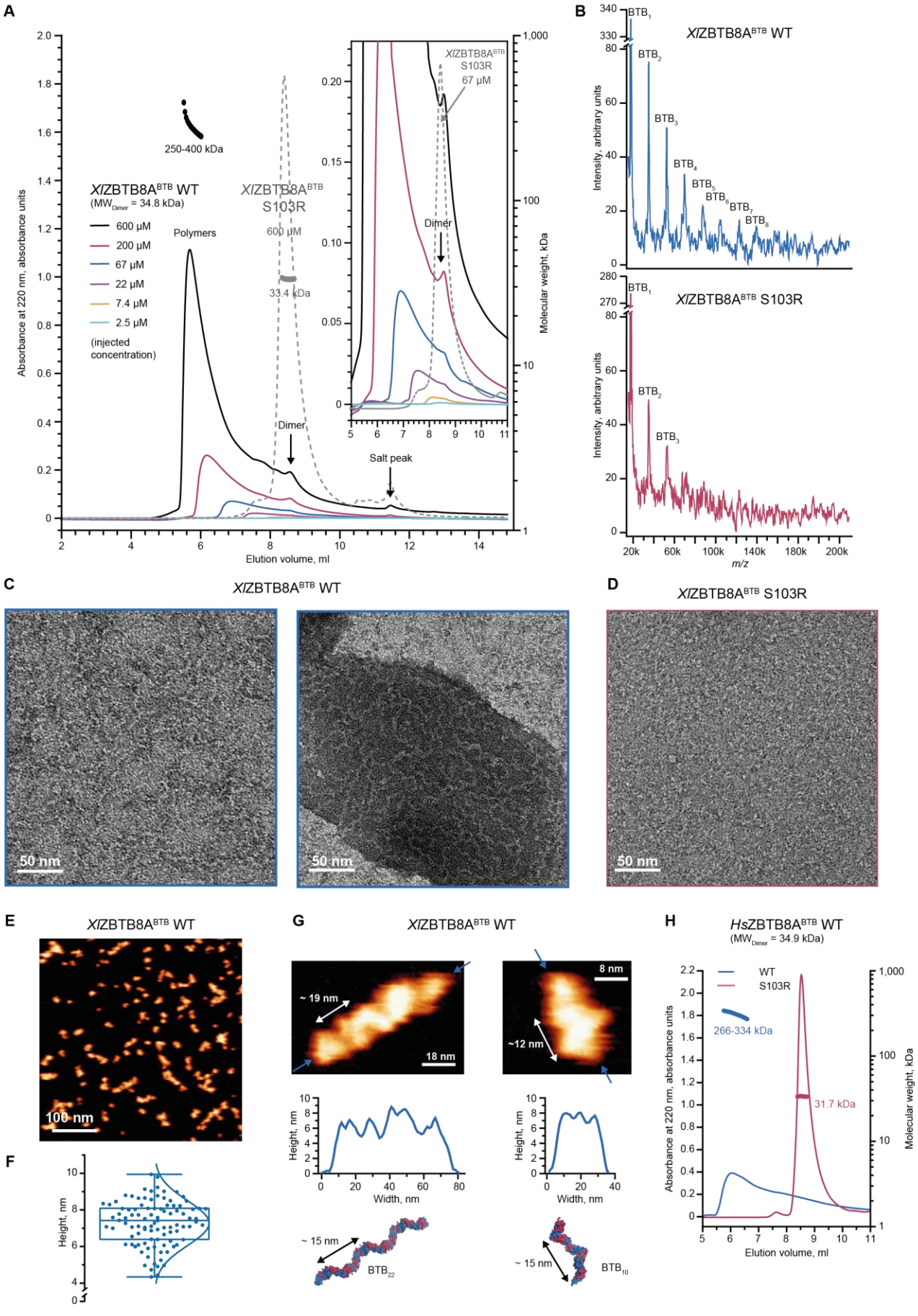
A
B
C
D
E
F
G
H
XlZBTB8A^BTB WT
(MW_Dimer = 34.8 kDa)
600 µM
200 µM
67 µM
22 µM
7.4 µM
2.5 µM
(injected concentration)
Polymers
Dimer
Salt peak
250-400 kDa
XlZBTB8A^BTB S103R
600 µM
33.4 kDa
67 µM
Absorbance at 220 nm, absorbance units
Elution volume, ml
Molecular weight, kDa
Intensity, arbitrary units
m/z
BTB1
BTB2
BTB3
BTB4
BTB5
BTB6
BTB7
BTB8
50 nm
100 nm
~ 19 nm
18 nm
8 nm
~12 nm
Height, nm
Width, nm
~ 15 nm
BTB22
BTB10
HsZBTB8A^BTB WT
(MW_Dimer = 34.9 kDa)
WT
S103R
266-334 kDa
31.7 kDa

Figure 3. Biophysical analysis of *Xl*ZBTB8A^{BTB} filaments

A SEC-RALS/LALS of *Xl*ZBTB8A^{BTB} WT and S103R. The MW of a dimer is provided. The inset shows a zoomed-in fragment. Thin lines correspond to UV and thick lines to apparent MW derived from light scattering.

B NALIM MALDI-TOF MS analysis of *Xl*ZBTB8A^{BTB} WT (top) and S103R (bottom) at 2.5 µM. BTB_n refers to a number of BTB domains in the indicated oligomer.

C Representative negative-stain electron micrographs of *Xl*ZBTB8A^{BTB} WT at 1.1 µM.

D Like C, but for the S103R mutant.

E Representative HS-AFM image of *Xl*ZBTB8A^{BTB} WT at 3 µM.

F Height distribution of the *Xl*ZBTB8A^{BTB}, box and whisker plot showing the median (line in the box), quartiles (edges of the box), and range (whiskers) over N = 101 particles.

G HS-AFM data for filaments of *Xl*ZBTB8A^{BTB} WT, including: the zoomed-in images with white arrows indicating the apparent pitch and blue arrows indicating the longitudinal axis (*top*); the height profile along the longitudinal axis (*middle*); the structural model of the corresponding fragment of the crystal filament (*bottom*).

H SEC-RALS/LALS of *Hs*ZBTB8A^{BTB} WT and S103R at the starting concentration of 600 µM. The MW of a dimer is provided. Thin lines correspond to UV and thick lines to apparent MW derived from light scattering.

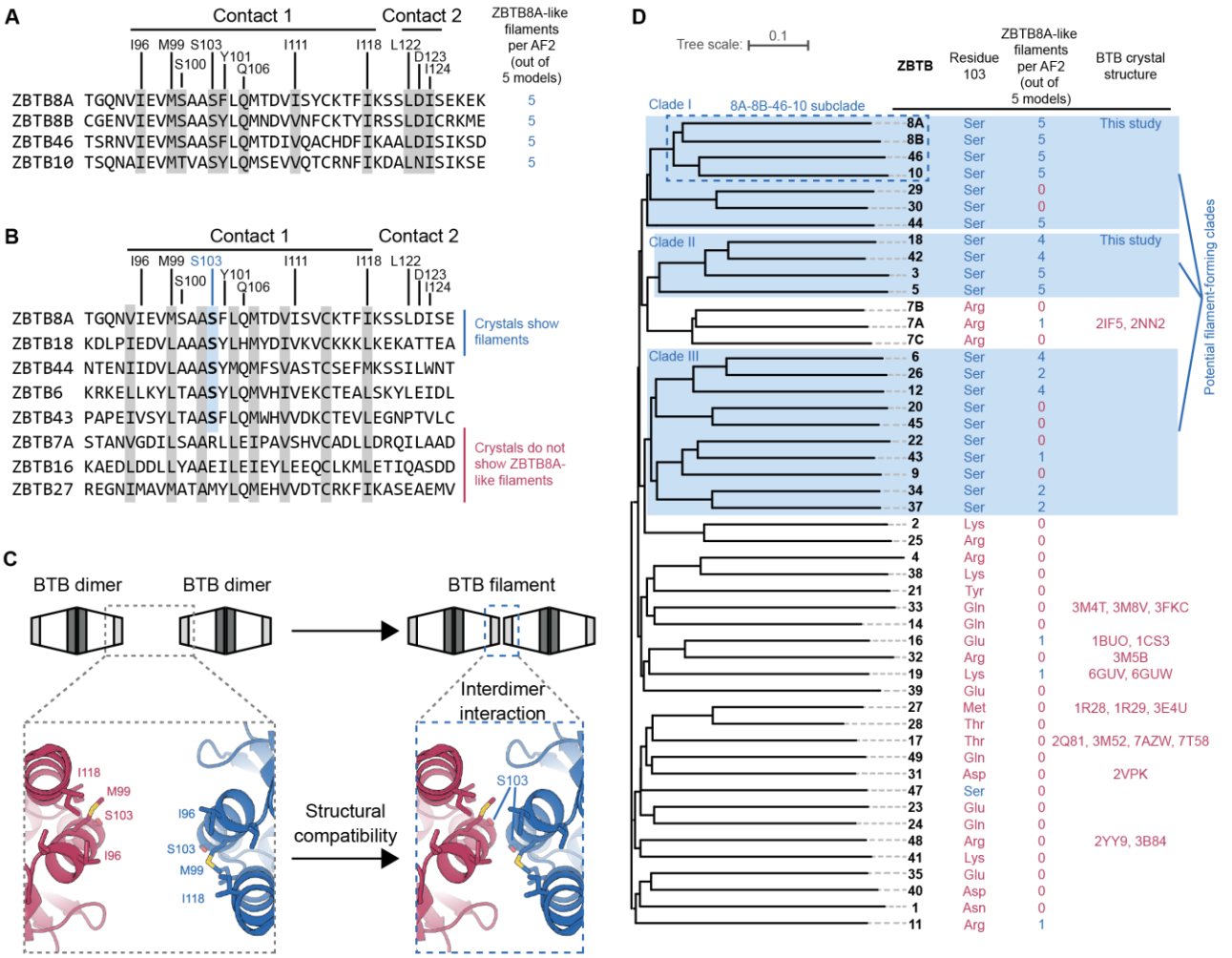

Figure 4. Phylogenetic analysis of the filamentation propensity within human ZBTB family

A A fragment of a multiple sequence alignment of *Hs*ZBTB8A with the indicated human ZBTB proteins and the results of AlphaFold2 modelling of interdimer contacts consistent with ZBTB8A-like BTB filaments. Residues are numbered according to ZBTB8A sequence

B Like in A but with human ZBTB proteins more distantly related to ZBTB8A and without AlphaFold2 modelling results

C The interdimer interaction requires structural compatibility between two copies of the contact 1 surface, which depends on a small amino-acid sidechain in position 103.

D A tentative phylogenetic tree of human ZBTB proteins. The inidividual observations indicative or not of the formation of ZBTB8A-like BTB-domain filaments are given in blue or red text, respectively. The whole clades considered as likely forming such filaments are highlighted with light blue boxes. PDB identifiers of published structures are provided.

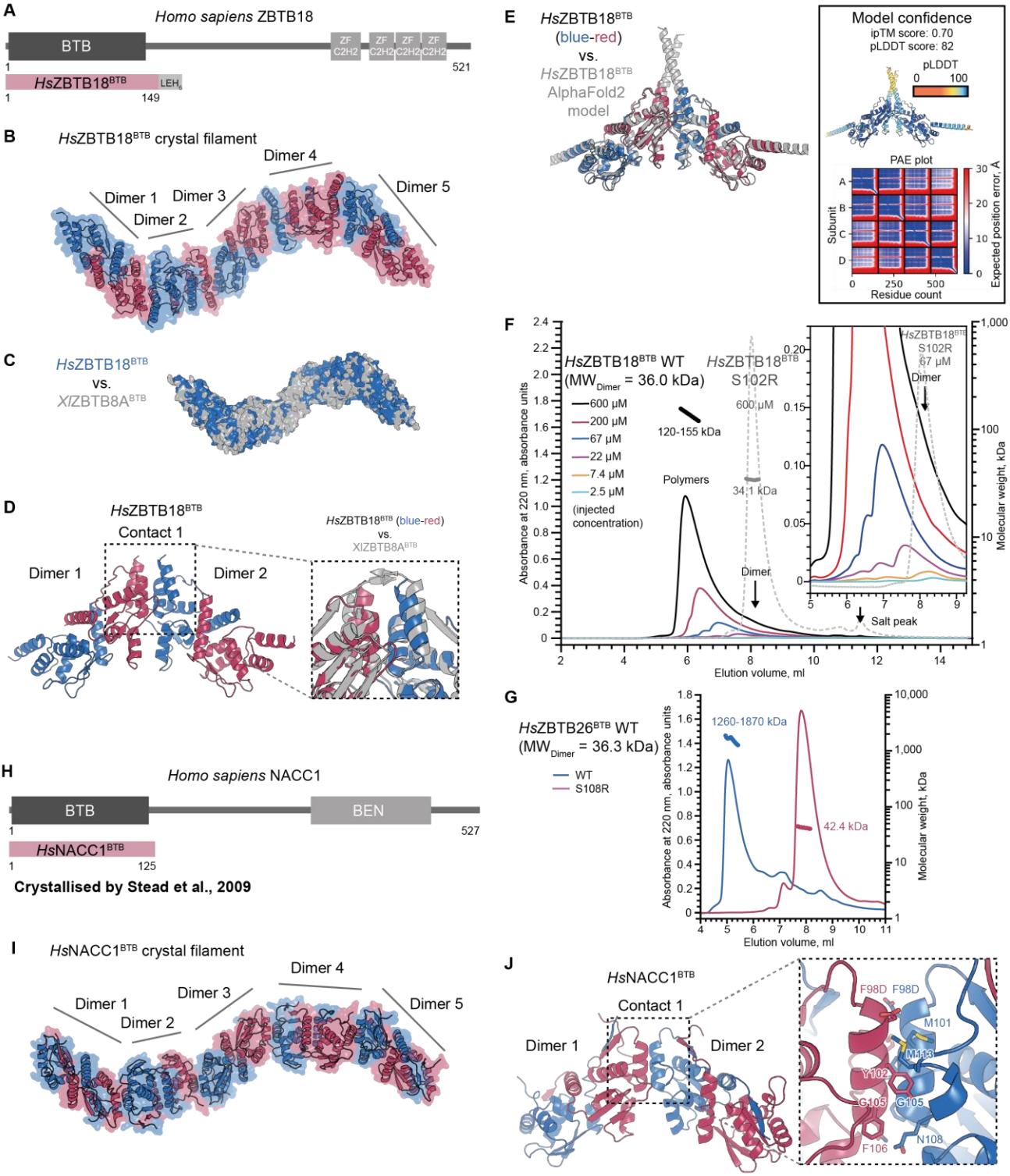
A
Homo sapiens ZBTB18
BTB
ZF C2H2
ZF C2H2
ZF C2H2
ZF C2H2
1
521
HsZBTB18BTB
LEHx
1
149
B
HsZBTB18BTB crystal filament
Dimer 1
Dimer 2
Dimer 3
Dimer 4
Dimer 5
C
HsZBTB18BTB
vs.
XlZBTB8ABTB
D
HsZBTB18BTB
Contact 1
Dimer 1
Dimer 2
HsZBTB18BTB (blue-red)
vs.
XlZBTB8ABTB
E
HsZBTB18BTB
(blue-red)
vs.
HsZBTB18BTB
AlphaFold2
model
Model confidence
ipTM score: 0.70
pLDDT score: 82
pLDDT
0
100
PAE plot
Subunit
A
B
C
D
0
250
500
Residue count
30
20
10
0
Expected position error, Å
F
HsZBTB18BTB WT
(MWDimer = 36.0 kDa)
HsZBTB18BTB
S102R
600 µM
200 µM
67 µM
22 µM
7.4 µM
2.5 µM
(injected
concentration)
120-155 kDa
Polymers
34.1 kDa
Dimer
600 µM
HsZBTB18BTB
S102R
67 µM
Dimer
Salt peak
Absorbance at 220 nm, absorbance units
Elution volume, ml
Molecular weight, kDa
G
HsZBTB26BTB WT
(MWDimer = 36.3 kDa)
WT
S108R
1260-1870 kDa
42.4 kDa
Absorbance at 220 nm, absorbance units
Elution volume, ml
Molecular weight, kDa
H
Homo sapiens NACC1
BTB
BEN
1
527
HsNACC1BTB
1
125
Crystallised by Stead et al., 2009
I
HsNACC1BTB crystal filament
Dimer 1
Dimer 2
Dimer 3
Dimer 4
Dimer 5
J
HsNACC1BTB
Contact 1
Dimer 1
Dimer 2
F98D
F98D
M101
M113
Y102
G105
G105
F106
N108

Figure 5. Filamentation of *Hs*ZBTB18^{BTB}, *Hs*ZBTB26^{BTB}, and *Hs*NACC1^{BTB}

A Domain architecture of human ZBTB18 and the crystallised fragment

B A fragment of the *Hs*ZBTB18^{BTB} filament observed in the crystal

C Structural superposition of fragments of *Hs*ZBTB18^{BTB} and *Xl*ZBTB8A^{BTB} filaments

D Crystal strucutre of the *Hs*ZBTB18^{BTB} interdimer contacts. The zoomed-in view shows a superposition of the interdimer assembly from the *Hs*ZBTB18^{BTB} and *Xl*ZBTB8A^{BTB} crystals.

E Comparison of *Hs*ZBTB18^{BTB} interdimer assembly from crystal structure and AlphaFold2 model. AlphaFold2 model coloured according to model confidence (pLDDT) and the PAE plot are inset.

F SEC-RALS/LALS at different starting concentration like in Figure 3A but now performed for *Hs*ZBTB18^{BTB} WT and S102R. The MW of a dimer is provided. Thin lines correspond to UV and thick lines to apparent MW derived from light scattering.

G SEC-RALS/LALS of *Hs*ZBTB26^{BTB} WT and S108R like in F but at a single starting concentration of 600 µM

H Domain architecture of human NACC1 and its previously crystallised fragment (PDB 3GA1)

I A fragment of the *Hs*NACC1^{BTB} F96D filament

J Interdimer contacts visible in the *Hs*NACC1^{BTB} F96D crystal

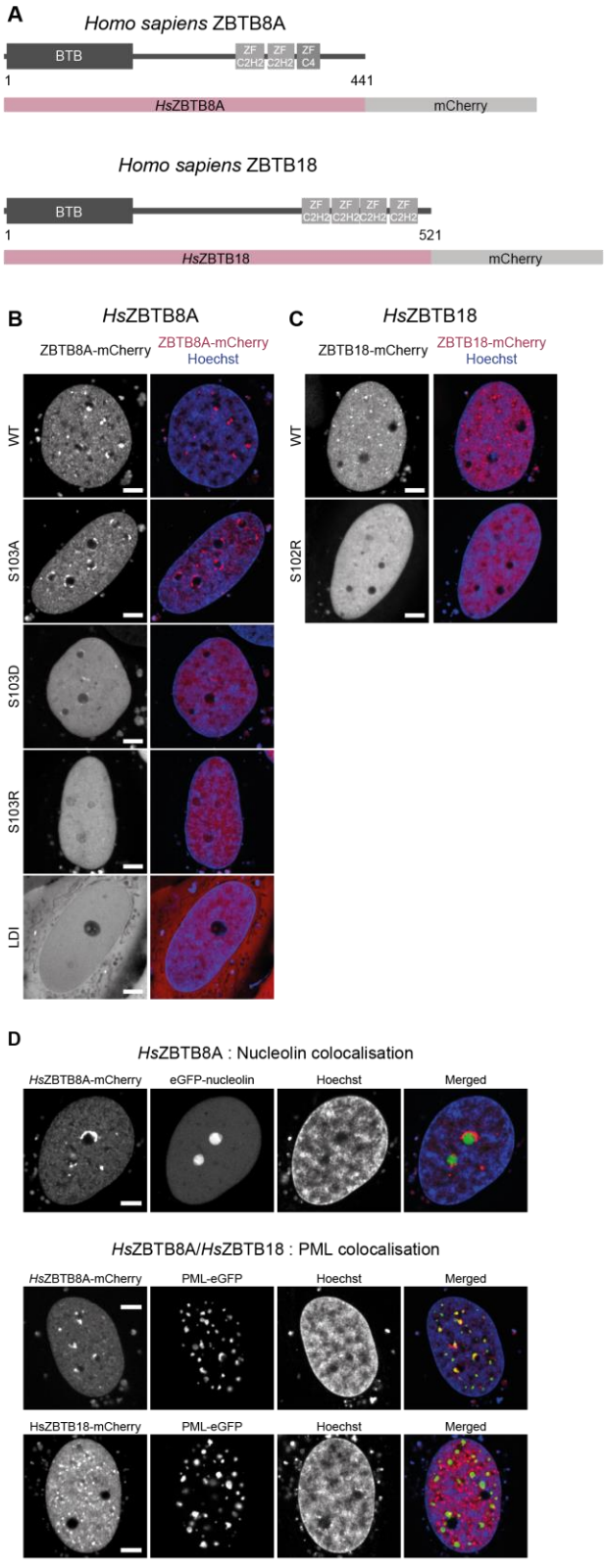
A
Homo sapiens ZBTB8A
BTB
ZF C2H2
ZF C2H2
ZF C4
1
441
HsZBTB8A
mCherry
Homo sapiens ZBTB18
BTB
ZF C2H2
ZF C2H2
ZF C2H2
ZF C2H2
1
521
HsZBTB18
mCherry
B
HsZBTB8A
ZBTB8A-mCherry
ZBTB8A-mCherry Hoechst
WT
S103A
S103D
S103R
LDI
C
HsZBTB18
ZBTB18-mCherry
ZBTB18-mCherry Hoechst
WT
S102R
D
HsZBTB8A : Nucleolin colocalisation
HsZBTB8A-mCherry
eGFP-nucleolin
Hoechst
Merged
HsZBTB8A/HsZBTB18 : PML colocalisation
HsZBTB8A-mCherry
PML-eGFP
Hoechst
Merged
HsZBTB18-mCherry
PML-eGFP
Hoechst
Merged
E
HsZBTB8A
(HsZBTB8A-mCherry)
Fluorescence
Low High
Before
+0.05 s
+0.2 s
+1.6 s
WT
inside foci
S103R
F
HsZBTB8A
(HsZBTB8A-mCherry)
Normalised fluorescence, %
100
80
60
40
20
0
0
1
2
3
6
7
Time after bleaching, s
WT inside foci
S103R
G
HsZBTB18
(HsZBTB18-mCherry)
Fluorescence
Low High
Before
+0.05 s
+0.2 s
+1.6 s
WT
inside foci
WT
outside foci
S102R
H
HsZBTB18
(HsZBTB18-mCherry)
Normalised fluorescence, %
100
80
60
40
20
0
0
1
2
3
6
7
Time after bleaching, s
WT inside foci
WT outside foci
S102R

Figure 6. Filamentation-dependent localisation of ZBTB proteins to dynamic foci

All scalebars correspond to 5 µm

A Domain architecture of human ZBTB8A and ZBTB18 and the mCherry-tagged constructs

B Representative confocal images of cells expressing either WT or mutant *Hs*ZBTB8A-mCherry, counterstained with Hoechst

C Like B but for *Hs*ZBTB18-mCherry

D Representative confocal images of cells coexpressing the indicated mCherry-tagged ZBTB protein and an eGFP-tagged form of either Nucleolin or PML isoform 4. In the merged image, the mCherry tag is in red, the eGFP tag is in green, the colocalisation of mCherry and eGFP tags in yellow, and Hoechst in blue.

E Representative time-course images of the fluorescence recovery after photobleaching (FRAP) of a circular area within the nucleus expressing *Hs*ZBTB8A-mCherry (WT or S103R). A representative bleached region is enlarged in an inset, with fluorescence coloured according to the indicated scale.

F Normalised FRAP curves for E. Mean and standard error of the mean for $N = 16$ (for WT) or 17 (for S103R) cells are shown

G An analysis equivalent to E but performed for *Hs*ZBTB18-mCherry (WT or S102R)

H Normalised FRAP curves for G. Mean and standard error of the mean for $N = 16$ cells are shown

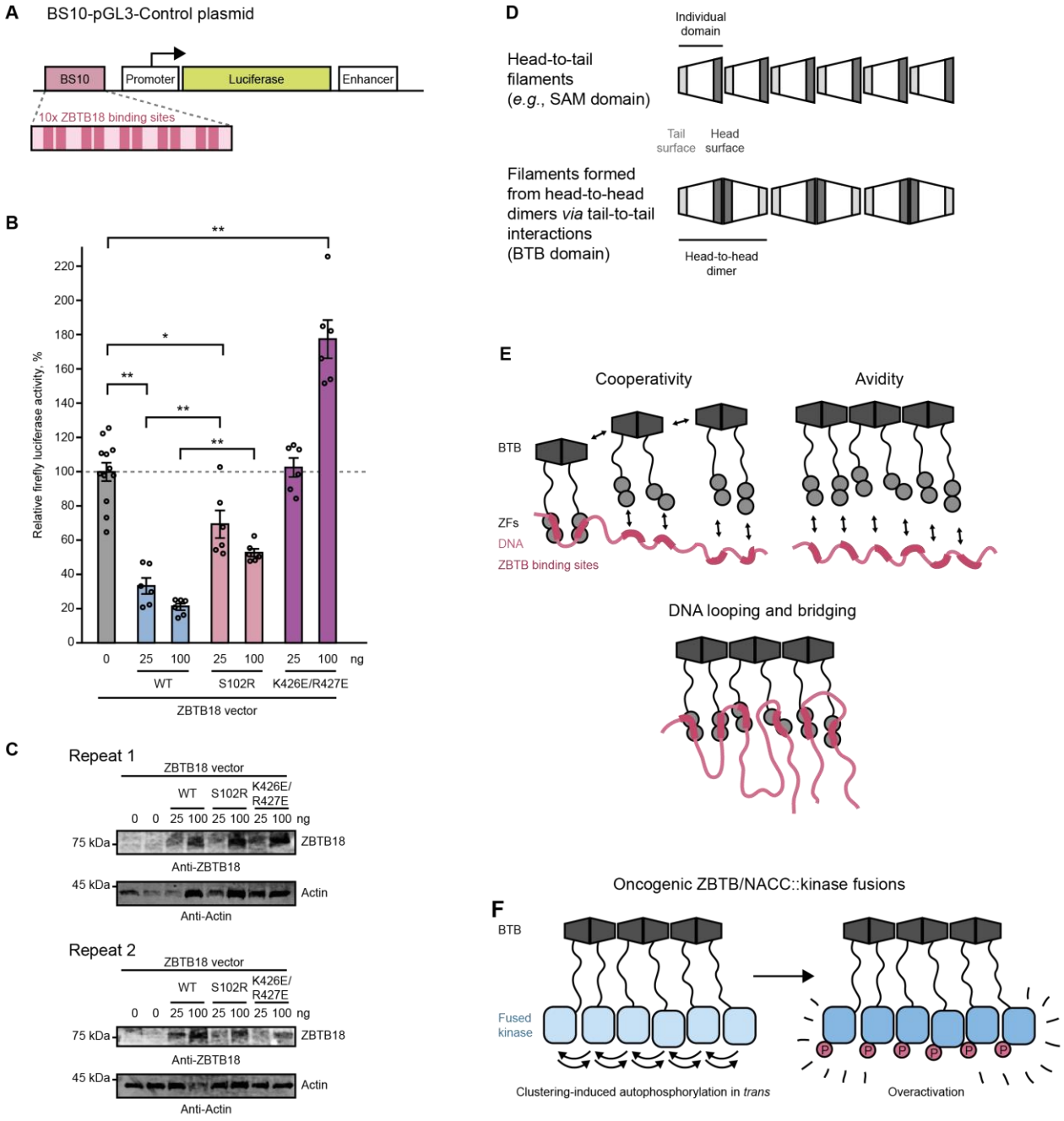
A
BS10-pGL3-Control plasmid
BS10
Promoter
Luciferase
Enhancer
10x ZBTB18 binding sites
B
Relative firefly luciferase activity, %
0 25 100 25 100 25 100 ng
WT
S102R
K426E/R427E
ZBTB18 vector
C
Repeat 1
ZBTB18 vector
WT S102R K426E/R427E
0 0 25 100 25 100 25 100 ng
75 kDa
ZBTB18
Anti-ZBTB18
45 kDa
Actin
Anti-Actin
Repeat 2
ZBTB18 vector
WT S102R K426E/R427E
0 0 25 100 25 100 25 100 ng
75 kDa
ZBTB18
Anti-ZBTB18
45 kDa
Actin
Anti-Actin
D
Individual domain
Head-to-tail filaments (e.g., SAM domain)
Tail surface
Head surface
Filaments formed from head-to-head dimers via tail-to-tail interactions (BTB domain)
Head-to-head dimer
E
Cooperativity
Avidity
BTB
ZFs
DNA
ZBTB binding sites
DNA looping and bridging
F
Oncogenic ZBTB/NACC::kinase fusions
BTB
Fused kinase
Clustering-induced autophosphorylation in trans
Overactivation

Figure 7. Functional importance and mechanistic models of BTB domain-mediated ZBTB clustering

A Firefly luciferase reporter plasmid. Promoter and enhancer sequences are derived from SV40.

B Luciferase reporter assay. Firefly luciferase luminescence was normalised against renilla luciferase luminescence and against the firefly luciferase activity without ZBTB18 vector. The results of $N = 12$ biological repeats for the control without ZBTB18 vector and $N = 6$ for all the other samples, the mean, and the standard error of the mean are shown. ** signifies $p < 0.01$. See Figure S2 for an analysis of endogenous target genes.

C ZBTB18 protein levels in two representative biological repeats of experiment shown in B probed through immunoblotting

D A comparison of the topologies of different dynamic filaments

E Tentative mechanisms for enhanced DNA binding enabled by dynamic BTB-domain filamentation. Nucleosomes are omitted for simplicity

F Proposed mechanism of the oncogenic action of fusions between ZBTB or NACC proteins and kinases

Table 1: X-ray data collection and refinement statistics

Radiation source	PROXIMA 1			PROXIMA 2	PROXIMA 1
Wavelength (Å)	0.97856			0.98012	0.97856
	ZBTB8A				**ZBTB18**
	Wild type	**S103R**	**S103D**	**S103A**	**Wild type**
Space group	$P4_132$	$P6_1$	$C2$	$P4_132$	$I4_1$
cell dimensions: *a, b, c* (Å)	153.70, 153.70, 153.70	87.92, 87.92, 97.80	260.00, 62.00, 71.49	154.15, 154.15, 154.15	188.91, 188.91, 139.09
α, β, γ (°)	90.00, 90.00, 90.00	90.00, 90.00, 120.00	90.00, 91.52, 90.00	90.00, 90.00, 90.00	90.00, 90.00, 90.00
No of molecules/asymmetric unit	2	2	6	2	8
Resolution range (Å)	48.60-3.10 (3.31-3.10)	48.90-1.85 (1.89-1.85)	129.96-3.75 (3.81-3.75)	48.75-3.72 (4.16-3.72)	57.36-4.15 (4.22-4.15)
Total observations	772655 (137482)	767642 (44985)	77342 (3142)	134481 (39002)	260945 (12546)
Unique reflections	11832 (2074)	36642 (2244)	11929 (547)	7053 (1944)	18588 (886)
Completeness (%)	100.0 (100.0)	100.0 (100.0)	99.7 (93.7)	99.9 (100.0)	100.0 (100.0)
Multiplicity	65.3 (66.3)	20.9 (20.0)	6.5 (5.7)	19.1 (20.1)	14.0 (14.2)
R_{pim} (%)	2.9 (75.1)	4.4 (43.2)	12.9 (77.7)	4.7 (41.1)	4.1 (47.2)
$I/\sigma(I)$	16.0 (1.2)	9.6 (1.4)	4.5 (1.2)	10.4 (2.0)	8.9 (1.4)
$CC_{1/2}$ (%)	99.9 (63.0)	99.5 (80.1)	91.4 (79.8)	99.9 (78.6)	99.8 (62.8)
Resolution range (Å)	48.60-3.10	35.48-1.85	71.46-3.75	44.50-3.72	57.36-4.15
Number of reflections used	11780	36567	11856	7019	18572
R_{work} / R_{free} (%)	24.01/26.35	17.03/18.81	24.64/29.54	26.34/28.97	34.58/35.99
Average B values (Å^2)					
All atoms	122.18	39.83	145.71	142.00	134.19
Protein chain A atoms	124.30	39.32	122.66	142.30	132.14
Protein chain B atoms	120.03	38.55	121.79	141.71	132.48
Protein chain C atoms	-	-	157.22	-	142.94
Protein chain D atoms	-	-	150.28	-	134.51
Protein chain E atoms	-	-	162.76	-	133.99
Protein chain F atoms	-	-	160.94	-	125.42
Protein chain G atoms	-	-	-	-	141.79
Protein chain H atoms	-	-	-	-	130.52
Ethylene glycol atoms	-	46.43	-	-	-
Water atoms	-	47.78	-	-	-
RMSD from ideality					
Bond lengths (Å)	0.002	0.007	0.001	0.001	0.003
Bond angles (°)	0.374	0.741	0.307	0.318	0.626
Ramachandran analysis					
Favoured / Allowed / Outliers (%)	98.4/1.6/0.0	98.3/1.7/0.0	96.6/3.4/0.0	96.7/3.3/0.0	94.4/5.0/0.6
Number of atoms					
Chain A	915	971	894	902	598
Chain B	900	951	882	891	603
Chain C	-	-	853	-	598
Chain D	-	-	865	-	603

Chain E	-	-	855	-	593
Chain F	-	-	877	-	593
Chain G	-	-	-	-	574
Chain H	-	-	-	-	598
Ethylene glycol	-	36	-	-	-
Water	-	185	-	-	-
PDB code	8P2N	8P2O	8RIT	8RIR	8P2P

Supplementary items

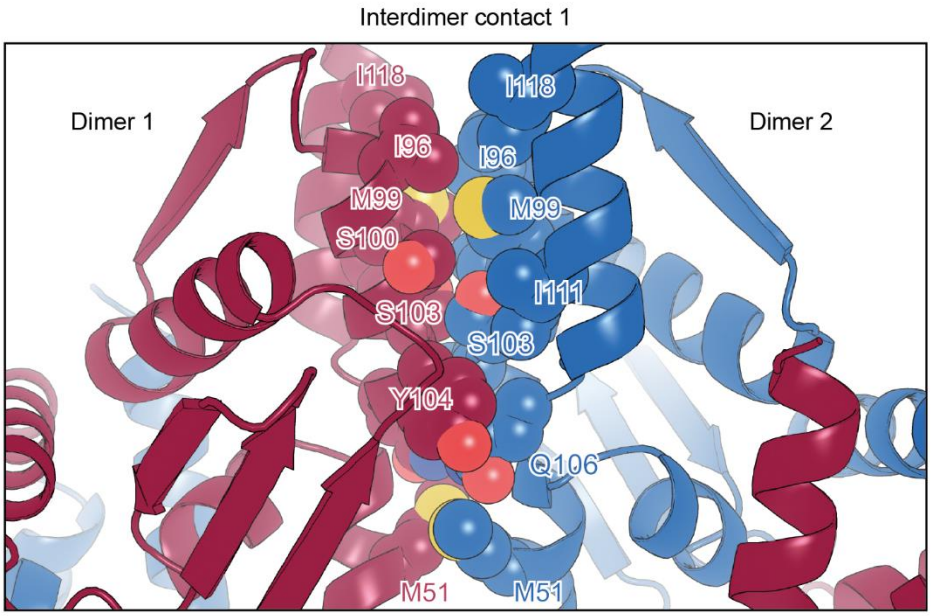

Figure S1. The interdimer contact 1, related to Figure 2A

A view of the interdimer interaction interface with zoomed-in contact 2 (see **Figure 2A** for an enlarged view). Sidechain atoms are shown as spheres, with carbon atoms coloured dark red or blue depending on the chain, oxygen atoms coloured light red, and sulphur atoms coloured yellow.

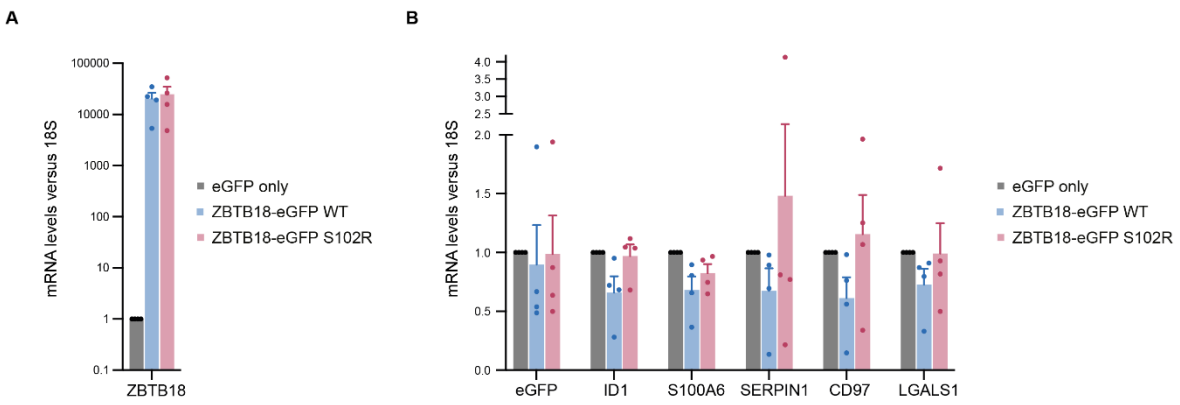

Figure S2. The effect of ZBTB18-eGFP overexpression on the expression of endogenous target genes probed with quantitative reverse-transcription polymerase chain reaction (RT-qPCR), related to Figure 7B

Primers used for the analysis are listed in **Table S2**.

A RT–qPCR results showing the overexpression of ZBTB18 in U2OS cells transfected with plasmids expressing eGFP, *Hs*ZBTB18-eGFP WT, and *Hs*ZBTB18-eGFP S102R. Gene expression was normalized to 18S rRNA and subsequently to the endogenous ZBTB18 expression level in cells transfected with eGFP-only plasmid treated as 1. *N* = 4 biological replicates. Individual results, mean, and standard error of the mean are shown.

B RT–qPCR results showing the expression of ZBTB18 target genes upon eGFP, *Hs*ZBTB18-eGFP WT, and *Hs*ZBTB18-eGFP S102R overexpression in U2OS cells. Gene expression was normalized to 18S rRNA and subsequently to the expression level of a given gene in cells transfected with GFP-only plasmid. *N* = 4 biological replicates. Individual results, mean and standard error of the mean are shown.

Table S1: Protein regions used for AlphaFold2 modelling of BTB interdimer interactions, related to STAR Methods

ZBTB	UniProtKB idenitifer/name	Analysed region
ZBTB1	Q9Y2K1/ZBTB1_HUMAN	1-137
ZBTB2	Q8N680/ZBTB2_HUMAN	1-130
ZBTB3	Q9H5J0/ZBTB3_HUMAN	51-186
ZBTB4	Q9P1Z0/ZBTB4_HUMAN	1-185
ZBTB5	O15062/ZBTB5_HUMAN	1-130
ZBTB6	Q15916/ZBTB6_HUMAN	1-137
ZBTB7A/LRF	O95365/ZBT7A_HUMAN	1-140
ZBTB7B	O15156/ZBT7B_HUMAN	1-155
ZBTB7C	A1YPR0/ZBT7C_HUMAN	1-141
ZBTB8A	Q96BR9/ZBT8A_HUMAN	1-129
ZBTB8B	Q8NAP8/ZBT8B_HUMAN	1-130
ZBTB9	Q96C00/ZBTB9_HUMAN	1-147
ZBTB10	Q96DT7/ZBT10_HUMAN	341-472
ZBTB11	O95625/ZBT11_HUMAN	181-325
ZBTB12	Q9Y330/ZBT12_HUMAN	1-137
ZBTB14/ZFP161	O43829/ZBT14_HUMAN	1-145
ZBTB16/PLZF	Q05516/ZBT16_HUMAN	1-135
ZBTB17/MIZ1	Q13105/ZBT17_HUMAN	1-145
ZBTB18/ZNF238/RP58	Q99592/ZBT18_HUMAN	1-125
ZBTB19/PATZ1/ZNF278	Q9HBE1/PATZ1_HUMAN	1-170
ZBTB20	Q9HC78/ZBT20_HUMAN	74-200
ZBTB21/ZNF295	Q9ULJ3/ZBT21_HUMAN	1-140
ZBTB22	O15209/ZBT22_HUMAN	1-155
ZBTB23/GZF1	Q9H116/GZF1_HUMAN	1-140
ZBTB24	O43167/ZBT24_HUMAN	1-140
ZBTB25	P24278/ZBT25_HUMAN	1-160
ZBTB26	Q9HCK0/ZBT26_HUMAN	1-138
ZBTB27/BCL6/ZNF51	P41182/BCL6_HUMAN	1-140
ZBTB28/BCL6B/ZNF6	Q8N143/BCL6B_HUMAN	1-142
ZBTB29/HIC1/ZNF901	Q14526/HIC1_HUMAN	1-159

ZBTB30/HIC2/ZNF907	Q96JB3/HIC2_HUMAN	1-151
ZBTB31/MYNN/ZNF902	Q9NPC7/MYNN_HUMAN	1-130
ZBTB32	Q9Y2Y4/ZBT32_HUMAN	1-130
ZBTB33/Kaiso	Q86T24/KAISO_HUMAN	1-140
ZBTB34	Q8NCN2/ZBT34_HUMAN	1-137
ZBTB35/ZNF131	P52739/ZN131_HUMAN	1-130
ZBTB37	Q5TC79/ZBT37_HUMAN	1-137
ZBTB38	Q8NAP3/ZBT38_HUMAN	1-132
ZBTB39	O15060/ZBT39_HUMAN	1-141
ZBTB40	Q9NUA8/ZBT40_HUMAN	1-130
ZBTB41	Q5SVQ8/ZBT41_HUMAN	61-195
ZBTB42	B2RXF5/ZBT42_HUMAN	1-130
ZBTB43/ZNF297B	O43298/ZBT43_HUMAN	1-137
ZBTB44	Q8NCP5/ZBT44_HUMAN	1-140
ZBTB45	Q96K62/ZBT45_HUMAN	1-135
ZBTB46/BZEL	Q86UZ6/ZBT46_HUMAN	1-136
ZBTB47	Q9UFB7/ZBT47_HUMAN	1-125
ZBTB48/TZAP	P10074/TZAP_HUMAN	1-130
ZBTB49	Q6ZSB9/ZBT49_HUMAN	1-130

Table S2: Primer sequences used in RT-qPCR experiments, related to Figure S2 and STAR Methods

Gene	Forward primer sequence	Reverse primer sequence
ZBTB18	TCTGAGCGAGCAGAGACAC	GGTCCTTGTAAAAGAGGTGGAAA
18S rRNA	CGCCGCTAGAGGTGAAATTC	CTTTCGCTCTGGTCCGTCTT
GFP	AAGCAGAAGAACGGCATCAA	GGGGGTGTTCTGCTGGTAGT
SERPINE1	ATTCAAGCAGCTATGGGATTCAA	CTGGACGAAGATCGCGTCTG
CD97	CCTGTCCGGCACCTCATAG	CCATAGTGACGTTCTTGTCCC
ID1	CTGCTCTACGACATGAACGG	GAAGGTCCCTGATGTAGTCGAT
S100A6	GGGAGGGTGACAAGCACAC	AGCTTCGAGCCAATGGTGAG
LGALS1	TCGCCAGCAACCTGAATCTC	GCACGAAGCTCTTAGCGTCA

Table S3: Parameters obtained from fitting of SAXS data, related to Figure 1I and STAR Methods

n	$q_z(n)$	$I°(n)$
0	0	$14.8\ 10^{-5}$
1	0.041	$16.5\ 10^{-5}$
2	0.082	$9.35\ 10^{-5}$
3	0.123	$3.83\ 10^{-5}$

constant	$-19.4\ 10^{-5}$
r°	38.6 Ang

STAR★Methods

Key resources table

REAGENT or RESOURCE	SOURCE	IDENTIFIER
Antibodies		
Rabbit polyclonal anti-ZBTB18 (ZNF238)	Proteintech	Cat#12714-1-AP
Mouse monoclona anti-β-Actin-HRP	Santa Cruz Biotechnology	Cat#sc-81178
Goat anti-Rabbit IgG (H+L) Secondary Antibody, HRP	Thermo Fisher	Cat#65-6120
Bacterial and virus strains		
Rosetta 2(DE3) competent cells (*E. coli*)	Novagen	Cat# 71397
BL21(DE3) competent cells (*E. coli*)	Novagen	Cat# 69450
NEB 10-beta competent cells (*E. coli)*	New England Biolabs	Cat# C3019H
Chemicals, peptides, and recombinant proteins		
ReadyBlue Coomasie	Sigma-Aldrich	Cat# RSB
bis(sulfosuccinimidyl)suberate (BS3)	Sigma-Aldrich	Cat# S5799
Imidazole	Sigma-Aldrich	Cat# I202
IPTG	VWR	Cat# 367-93-1
X-tremeGENE 360 DNA transfection reagent	Roche	Cat# XTG360-RO
Dulbecco's modified Eagle's Medium (DMEM)	Gibco	Cat# 21969035
Phenol red–free Leibovitz's L-15 medium	Thermo Fisher	Cat# 11415064
Hoechst 33342	Thermo Fisher	Cat# 62249
Lipofectamine LTX Reagent with PLUS™ Reagent	Thermo Fisher	Cat# 15338030
Reduced serum medium I Opti-MEM™, without phenol red	Thermo Fisher	Cat# 11058-021
GlutaMAX	Thermo Fisher	Cat# 35050-061
Dulbecco's Modification of Eagle's Medium, 1x	Corning	Cat# 10-101-CV
Dual-Luciferase Reporter Assay System	Promega	Cat# E1910
4–20% Mini-PROTEAN TGX Stain-Free Protein Gels	BioRad	**Cat#**4568094
WesternBright ECL HRP substrate	Advansta	Cat# K-12045-D50
NucleoSpin RNA, Mini kit for RNA purification	Macherey-Nagel	Cat# 740955.50
RevertAid Reverse Transcriptase (200 U/µL)	Thermo Fisher	Cat# EP0441
Master Mix PCR Power SYBR Green	Thermo Fisher	Cat# 4368577
Deposited data		
Polymeric form of the BTB domain of ZBTB8A from *Xenopus laevis*	This study	PDB code: 8P2N
Dimeric mutant S103R of the BTB domain of ZBTB8A from *Xenopus laevis*	This study	PBD code: 8P2O
Polymeric form of the BTB domain of human ZBTB18	This study	PDB code: 8P2P
Dimeric mutant S103D of the BTB domain of ZBTB8A from *Xenopus laevis*	This study	PDB code: 8RIT
S103A mutant of the BTB domain of ZBTB8A from *Xenopus laevis*	This study	PDB code: 8RIR
The BTB domain (wild-type) of the zinc finger and BTB domain-containing protein 8A.1-A (ZBTB8A) from *Xenopus laevis*	This study	SASBDB code: SASDR98
The BTB domain (S103R mutant) of the zinc finger and BTB domain-containing protein 8A.1-A (ZBTB8A) from *Xenopus laevis*	This study	SASBDB code: SASDRA8

Mendeley Data dataset with uncropped gels, blots, and raw microscopy images	This study	2bkyy9vjpk
Experimental models: Cell lines		
Human: U2OS WT	Ivan Ahel laboratory	N/A
African green monkey: COS-7 WT	Béatrice Vallée-Méheust and Hélène Bénédetti laboratory	N/A
Oligonucleotides		
Table 3.	This study	N/A
Recombinant DNA		
pET-28a(+) HsZBTB8A-LEH6 1-146	This study	N/A
pET-21a(+) HsZBTB18-LEH6 1-149	This study	N/A
pET-21a(+) HsZBTB5-LEH6 1-137	This study	N/A
pET-21a(+) HsZBTB20-LEH6 74-232	This study	N/A
pET-24a(+) HsZBTB12-LEH6 1-137	This study	N/A
pET-24a(+) HsZBTB26-LEH6 1-150	This study	N/A
pET-21a(+) HsZBTB43-LEH6 1-149	This study	N/A
pET-28a(+) XlZBTB8A-LEH6 1-146	This study	N/A
pET-28a(+) MG-XlZBTB8A-LEH6 1-146	This study	N/A
pET-28a(+) XlZBTB8A-LEH6 1-146 S103R	This study	N/A
pET-28a(+) XlZBTB8A-LEH6 1-146 S103D	This study	N/A
pET-28a(+) XlZBTB8A-LEH6 1-146 S103A	This study	N/A
pET-28a(+) XlZBTB8A-LEH6 1-146 L122A/D123A/I124A or 'LDI'	This study	N/A
pET-28a(+) XlZBTB8A-LEH6 1-146 I96D	This study	N/A
pET-28a(+) XlZBTB8A-LEH6 1-146 M51R	This study	N/A
pET-28a(+) XlZBTB8A-LEH6 1-146 M51R/I96D/S103R/L122A/D123A/I124A or 'Multi'	This study	N/A
pET-28a(+) HsZBTB8A-LEH6 1-146 S103R	This study	N/A
pET-21a(+) HsZBTB18-LEH6 1-149 S102R	This study	N/A
pET-24a(+) HsZBTB26-LEH6 1-150 S108R	This study	N/A
pmCherry-N1 HsZBTB8A-mCherry 1-441	This study	N/A
pmCherry-N1 HsZBTB8A-mCherry 1-441 S103R	This study	N/A
pmCherry-N1 HsZBTB18-mCherry 1-522	This study	N/A
pmCherry-N1 HsZBTB18-mCherry 1-522 S102R	This study	N/A
pmCherry-N1 HsZBTB8A-mCherry 1-441 S103D	This study	N/A
pmCherry-N1 HsZBTB8A-mCherry 1-441 S103A	This study	N/A
pmCherry-N1 HsZBTB8A-mCherry 1-441 LDI	This study	N/A
pmCherry-N1 HsZBTB8A-mCherry 1-441 I96D	This study	N/A
eGFP-Nucleolin	Michael Kastan laboratory, via AddGene	Plasmid #28176
pEGFP-N1 PML isoform 4 1-633	This study	N/A
pEGFP-N1 ΔEGFP HsZBTB18 1-522	This study	N/A
pEGFP-N1 ΔEGFP HsZBTB18 1-522 S102R	This study	N/A
pEGFP-N1 ΔEGFP HsZBTB18 1-522 K426E/R427E	This study	N/A
BS10-pGL3-Control	This study	N/A
pRL-SV40	Promega	Cat# E2231
pET-28a(+) MGH6-UBC9 1-158	Goffinont et al., *JBC*, 2023	N/A
pEGFP-N1 HsZBTB18-EGFP 1-522	This study	N/A
pEGFP-N1 HsZBTB18-EGFP 1-522 S102R	This study	N/A
pEGFP-N1 GFP	This study	N/A

Software and algorithms		
XDS	Kabsch	https://xds.mr.mpg.de/
AIMLESS	Evans and Murshudov	https://www.ccp4.ac.uk/html/aimless.html
Phaser	McCoy	https://www-structmed.cimr.cam.ac.uk/phaser_obsolete/
Phenix	Adams et al.	https://phenix-online.org/download/
COOT	Emsley and Cowtan	https://www2.mrc-lmb.cam.ac.uk/personal/pemsley/coot/
MolProbity	Davis et al.	http://molprobity.biochem.duke.edu/
Protein Repair and Analysis Server	Nnyigide et al.	https://www.protein-science.com/
PyMOL, v. 2.6	Schrödinger and DeLano	https://pymol.org/2/
UCSF Chimera v. 1.17.3	Pettersen et al.	https://www.cgl.ucsf.edu/chimera/
PISA	Krissinel and Henrick	https://www.ebi.ac.uk/pdbe/pisa/
ConSurf server	Glaser et al.; Yariv et al.	https://consurf.tau.ac.il
FOXTROT	Girardot et al.	N/A
BioXTAS RAW	Hopkins et al.	https://sourceforge.net/projects/bioxtasraw/
GNOM (ATSAS)	Manalastas-Cantos et al.	https://www.embl-hamburg.de/biosaxs/download.html
BIFT (BioXTAS RAW)	Hansen	https://bioxtas-raw.readthedocs.io/en/latest/
Bruker FlexControl software v.4	Bruker	N/A
FlexAnalysis software v.4	Bruker	N/A
WsXM	Horcas et al.	N/A
UniProt	The UniProt Consortium	https://www.uniprot.org/
ClustalOmega	Sievers et al. ; Goujon et al	https://www.ebi.ac.uk/Tools/msa/clustalo/
Interactive Tree Of Life (iTOL) version 5	Letunic and Bork	https://itol.embl.de/
Adobe Illustrator CS6	Adobe	N/A
BLAST	Altschul	https://blast.ncbi.nlm.nih.gov/Blast.cgi?PAGE=Proteins
ColabFold; version 1.5.5	Mirdita et al.	https://colabfold.com
FIJI ImageJ	Schneider et al.	https://imagej.net/software/fiji/downloads
Other		
HisTrap HP column	Cytiva	Cat# 17-5248-01
HiTrap Q HP column	Cytiva	Cat# 17-1154-01
HiTrap SP HP column	Cytiva	Cat# 17-1152-01
HiLoad Superdex 75 16/600 column	Cytiva	Cat# 28-9893-33
HiLoad Superdex 200 16/600 column	Cytiva	Cat# 28-9893-35
Superdex 200 Increase 10/300 GL	Pharmacia/Cytiva	Cat# 28-9909-44
Mosquito liquid handler	TTP Labtech	N/A
Swissci MRC 96-Well 2-Drop Plates	Molecular Dimensions	Cat# MD11-00-100

BioSEC-3 300Å, 4.6 x 300 mm, 3 µm	Agilent	Cat# 5190-2513
AdvanceBio SEC 300Å, 7.8 x 300 mm, 2.7 µm	Agilent	Cat# PL1180-5301
Microplate, 96-Well, PS, F-bottom, clear	Greiner Bio-One	Cat# 655161
Microplate, 96-Well, PS, F-bottom, white	Dominique Dutscher	Cat# 2536723

Resource availability

Lead contact

Requests for information and reagents may be directed to and will be fulfilled by the Lead Contact Marcin J. Suskiewicz (marcin.suskiewicz@cnrs-orleans.fr).

Materials availability

All resources used for this study are available from the lead contact upon request.

Data and code availability

- Crystal structure coordinates and structure factors have been deposited in the Protein Data Bank (PDB) under the identifiers 8P2N, 8P2O, 8P2P, 8RIT, and 8RIR. SAXS data were deposited in Small Angle Scattering Biological Data Bank (SASBDB) under the identifiers SASDR98 and SASDRA8.No original code was generated in this study. Uncropped gels, blots, and raw microscopy images are deposited in a Mendeley Data repository 2bkyy9vjpk.
- This paper does not report original code.
- Any additional information required to reanalyse the data reported in this paper is available from the lead contact upon request.

Experimental model and study participant details

Bacterial strains

Escherichia coli NEB10-beta competent cells (New England BioLabs, cat. no. C3019H) were used for cloning, mutagenesis, and plasmid amplification. *E. coli* Rosetta 2 (DE3) or BL21 (DE3) competent cells (Novagen, cat. no. 71397 or 69450) were used for protein production. Cells were grown in Luria-Bertani/lysogeny broth (LB) cultures supplemented with an appropriate antibiotic in a shaking incubator at 37 °C unless otherwise indicated in method details.

Cell lines

U2OS WT cells were cultured in Dulbecco's modified Eagle's medium (DMEM; Sigma-Aldrich) supplemented with 10% fetal bovine serum (FBS), penicillin (100 U/ml), streptomycin (100 µg/ml), and 1% nonessential amino acid and maintained at 37 °C in a 5% CO2 incubator.

African green monkey kidney fibroblast-like cells (COS-7) were cultured in high glucose (4.5 g/L) DMEM medium supplemented with 10% fetal bovine serum (FBS), penicillin (100 U/ml), streptomycin (100 µg/ml), and 2 mM GlutaMAX and maintained at 37 °C in a 5% CO_2 incubator.

Method details

Plasmids for recombinant protein production

DNA sequences encoding BTB domains of the following human proteins were synthesised by GenScript in a codon-optimised form (for *Escherichia coli*): ZBTB8A (residues 1-146 of the Uniprot sequence Q96BR9|ZBT8A_HUMAN), ZBTB5 (residues 1-137 of O15062|ZBTB5_HUMAN), ZBTB18 (residues 1-149 of Q99592|ZBTB18_HUMAN), ZBTB20 (residues 74-232 of Q9HC78|ZBT20_HUMAN), ZBTB12 (residues 1-137 of Q9Y330|ZBT12_HUMAN), ZBTB26 (residues 1-150 of Q9HCK0|ZBT26_HUMAN), and ZBTB43 (residues 1-149 of O43298|ZBT43_HUMAN). Additionally, a codon-optimised DNA sequence encoding the BTB domain from an orthologue of ZBTB8A from *Xenopus laevis* (residues 1-146 of Q0IH98|ZB8AA_XENLA) was also synthesised.

These synthetic inserts were cloned into pET-28a, pET-21a, or pET-24a plasmids in a way that conferred on the protein product a C-terminal -LEHHHHHH tag and no extension at the N terminus, except for *Xl*ZBTB8A^{BTB}, for which we produced plasmids encoding the protein both without and with an N-terminal MG- extension. *Xl*ZBTB8A^{BTB} with the MG- extension was used for crystal structure determination, while the variant without the extension was used for all other experiments.

Point mutations were introduced using a standard mutagenesis PCR reaction followed by DpnI treatment.

Plasmids for cellular analyses

Coding DNA sequences corresponding to full-length human ZBTB8A (Q96BR9|ZBT8A_HUMAN, CCDS30664.1) and ZBTB18 (Q99592|ZBTB18_HUMAN, CCDS1622.1) proteins were synthesised by GeneCust without codon optimisation. The inserts were flanked by XhoI and BamHI sites at 5’ and 3’ ends, respectively. These two restriction enzymes were used to clone the inserts into a pmCherry-N1 vector, generating *Hs*ZBTB8A-mCherry WT and *Hs*ZBTB18-mCherry WT plasmids.

To create untagged *Hs*ZBTB8A and *Hs*ZBTB18 plasmids for the luciferase reporter assay, first the inserts from the above paragraphs were pasted into pEGFP-N1 vectors, and then eGFP was deleted using standard site-directed mutagenesis.

Coding DNA sequence of PML isoform 4 (P29590-5, CCDS45297.1) was synthesised by GeneCust without codon optimisation, flanked by XhoI and BamHI sites, and cloned into pEGFP-N1 vector using these enzymes.

pGL3-Control plasmid was created by pasting an SV40 enhancer sequence GGATCCTGAACGATGGAGCGGAGAATGGGCGGAACTGGGCGGAGTTAGGGGCGGGA TGGGCGGAGTTAGGGGCGGGACTATGGTTGCTGACTAATTGAGATGCATGCTTTGCA TACTTCTGCCTGCTGGGGAGCCTGGGGACTTTCCACACCTGGTTGCTGACTAATTGAG ATGCATGCTTTGCATACTTCTGCCTGCTGGGGAGCCTGGGGACTTTCCACACCCTAAC TGACACACATTCCACAGCGTCGAC synthesised by GeneCust into a pGL3-Promoter plasmid using BamHI and SalI restriction sites. Then, to create the BS10-pGL3-Control plasmid, we pasted, into this pGL3-Control plasmid, the 'BS10' sequence GAGCTCCACGCGGTGGCGGCGCTCTAGAATAGTGGATCCATTGCAGATGTTCAACAT CTGGGTCGCTGTAGGAATTCCTACAGGCGCAACATCTGGCCAGATGTGCAATGGATC CATTGCAGATGTTGCCAGATGTTTTCGCTGTAGGAATTCCTACAGCCAGATGTGTCCA

GATGTGCAATGGATCCATTGCAGATGTTGCCAGATGTTTTCGCTGTAGGAATTCGATAT CAAGCTTATCGATACCGTCGACCTCGAGGGGGGGCCCGGTACC, which was derived from a previous study[9] and synthesised by GeneCust. This sequence was inserted in reverse using KpnI and SacI restriction sites.

Standard site-directed mutagenesis was used to create all point mutants. The plasmids were amplified in bacteria and isolated.

Expression and purification of recombinant proteins

All proteins except for UBC9 were expressed and purified according to the same protocol. An expression plasmid was transformed into *E. coli* Rosetta 2 (DE3) or BL21 (DE3) competent cells (Novagen, cat. no. 71397 or 69450). Cells were grown in 2-l LB cultures supplemented with ampicillin or kanamycin at 37 °C. The expression was induced with 0.5 mM isopropylthio-β-galactoside (IPTG) when the OD_{600} reached ~0.9. Following overnight expression at 20 °C, cells were harvested by centrifugation (4,000 g for 40 min at 15 °C) and resuspended in HisTrap buffer (25 mM HEPES, pH 7.5, 200 mM NaCl, 5% glycerol, and 0.5 mM tris(2-carboxyethyl)phosphine (TCEP)). Lysis was performed by 1-h incubation with lysozyme (0.5 mg/ml) and benzonase (15 U/ml) at room temperature, followed by sonication. Crude lysates were clarified by centrifugation (15,000 g for 1 h at 15 °C), at which stage proteins were divided into pellet and supernatant.

Supernatants were loaded onto a 5-ml HisTrap HP column (Cytiva, cat. no. 17-5248-01) equilibrated in HisTrap buffer. The column was washed with the same buffer first without and then with 50 mM imidazole, followed by protein elution with 500 mM imidazole. The elution was diluted 4-fold with water to decrease NaCl concentration and loaded onto a 5-ml HiTrap Q HP column (Cytiva, cat. no. 17-1154-01). The protein was eluted with a gradient of 50 mM to 1 M NaCl at pH 7.5, in a 25 mM HEPES buffer at pH 7.5, eluting around 300 mM NaCl. *Xl*ZBTB8A^{BTB} WT and *Hs*ZBTB18^{BTB} WT used for crystallisation, as well as HSZBTB26BTB WT and S108R, were additionally purified using a a HiLoad Superdex 75 or 200 prep grade 16/600 column (Cytiva, cat. no. 28-9893-33 or 28-9893-35) in 25 mM Tris (for *Hs*ZBTB18^{BTB}) or HEPES (for theall others), pH 7.5, 150 mM NaCl, 0.5 mM TCEP

Human/*Xenopus* (identical sequence) UBC9 was expressed and purified slightly differently from other protein. The expression using the pET-28a(+) MGH6-UBC9 1-158 plasmid[104] was carried out in *E. coli* BL21 (DE3) cells cultured in LB medium supplemented with kanamycin at 37 °C until an OD_{600} of ~0.9 and induced with 0.5 mM isopropylthio-β-galactoside (IPTG). After 3 h of expression, the cells were harvested and frozen. Defrosted cells were suspended in 500 mM NaCl, 25 mM HEPES, pH 7.5, 20 mM imidazole, 5% glycerol, 1 mM DTT supplemented with 0.5 mg/ml lysozyme, followed by sonication and centrifugation at 27,000 g for 30 min. The supernatant was loaded onto a 5-ml HisTrap HP column (Cytiva, cat. no. 17-5248-01) equilibrated in the same buffer. After loading, the column was washed with a buffer supplemented with 30 mM imidazole and eluted by an imidazole gradient of 30–200 mM over 100 ml. UBC9 was further purified by ion exchange using a 5-ml HiTrap SP HP column (Cytiva, cat. no. 17-1152-01) and SEC using a HiLoad Superdex 75 16/600 column (Cytiva, cat. no. 28-9893-33) in 200 mM NaCl, 20 mM HEPES, pH 7.5, 5% of glycerol, and 1 mM DTT.

Purified proteins were concentrated and analysed by SDS-polyacrylamide gel electrophoresis (SDS-PAGE) (16% acrylamide, run for 45 min at 210 V), followed by staining with ReadyBlue Coomassie (Sigma Aldrich, cat. no. RSB). Molecular weights of purified proteins were confirmed by MALDI mass spectrometry.

Size exclusion chromatography coupled with static light scattering (SEC-RALS/LALS)

Average molecular weight (MW) was determined by SEC-RALS/LALS using an Agilent 1260 Infinity HPLC system (Agilent, DE, USA) with a diode array detector coupled in series with a two-angle (15 and 90°) laser light-scattering and a refractive index detector. 10 µl of ZBTB samples at concentrations indicated in figures or figure legends were automatically injected into an Agilent AdvanceBio SEC 300A column (2.7 µm, 7.8 x 300 mm) equilibrated with filtered PBS buffer. Column temperature was set at 30°C and HPLC run time was 18 minutes for each injection, with a flow of 1 ml/min. All data were analysed using Agilent GPC/SEC software and a refractive index increment (dn/dC) of 0.185 ml/g was used for the calculation of the molecular weight of ZBTB samples.

Analytical size-exclusion chromatography (SEC) followed by SDS-PAGE

100-µl protein samples of *Xenopus laevis* ZBTB8A WT and different mutants at the concentration of 100 µM were injected onto an analytical Superdex 200 Increase 10/300 GL column (Pharmacia/Cytiva, cat. no. 28-9909-44) equilibrated in 1x Phosphate Buffered Saline (PBS, 137 mM NaCl, 2.7 mM KCl, 10 mM phosphate buffer, pH 7.4). 1-ml fractions were collected and analysed by SDS-PAGE.

BS3 crosslinking

Protein samples at 30 µM in 25 mM HEPES, pH 7.5, 150 mM NaCl, and 0.5 mM TCEP were incubated with 0.75 mM bis(sulfosuccinimidyl)suberate (BS3) at 25 °C for 30 minutes. The reactions were quenched by mixing the sample with 100 mM Tris at pH 7.6 at a 9:1 ratio. A 15-min incubation was followed by an SDS-PAGE analysis.

Crystallisation and X-ray structure determination

Crystallisation screening was performed using a Mosquito liquid handler (TTP Labtech) in Swissci MRC 96-Well 2-Drop Plates (Molecular Dimensions, cat. no. MD11-00-100) *via* a sitting-drop vapour-diffusion method in 200-nl drops composed of 1:1 mixture of protein and reservoir solution. Crystals were grown between 1 and 7 days at 20 °C.

Protein stocks used for crystallisation were at the following concentrations and in the following buffers: *Xl*ZBTB8A^{BTB} WT at 0.6 mM in 8 mM HEPES, pH 7.5, 50 mM NaCl, 0.16 mM TCEP; *Xl*ZBTB8A^{BTB} S103A at 0.7 mM in 25 mM HEPES, pH 7.5, 350 mM NaCl, 0.5 mM TCEP; *Xl*ZBTB8A^{BTB} S103D at 2.3 mM in 25 mM HEPES, pH 7.5, 350 mM NaCl, 0.5 mM TCEP; *Xl*ZBTB8A^{BTB} S103R at 1.6 mM in 25 mM HEPES, pH 7.5, 350 mM NaCl, 0.5 mM TCEP; *Hs*ZBTB18^{BTB} at 1.2 mM in 25 mM Tris, pH 7.5, 150 mM NaCl, 0.5 mM TCEP.

Crystals were obtained in the following conditions: *Xl*ZBTB8A^{BTB} WT: 100 mM Na/K phosphate pH 6.2, 200 mM NaCl, 50% *v*/*v* PEG200; *Xl*ZBTB8A^{BTB} S103A: 100 mM MES pH 6.5, 50 mM CsCl, 30% *v*/*v* Jeffamine M-600; *Xl*ZBTB8A^{BTB} S103D: 100 mM MES/imidazole pH 6.5, 20 mM 1,6-hexanediol, 20 mM 1-butanol, 20 mM (*RS*)-1,2-propanediol, 20 mM 2-propanol, 20 mM 1,4-butanediol, 20 mM 1,3-propanediol, 20% *v*/*v* ethylene glycol, 10 %

w/*v* PEG8000; *Xl*ZBTB8A^{BTB} S103R: 100 mM Na citrate pH 5.0, 8% *w*/*v* PEG8000; *Hs*ZBTB18^{BTB}: 200 mM MgCl2, 1 M imidazole pH 7.5, 20% *v*/*v* EtOH.

For *Xl*ZBTB8A^{BTB} WT, we attempted to crystallise two protein variants, one with and one without an MG- extension at the N terminus. Moreover, in addition to these *Xl*ZBTB8A^{BTB} variants alone, we also tried crystallising them in a stoichiometric mixture (0.6 mM each) with UBC9. This was motivated by a hypothesis that UBC9 might be an interactor of ZBTB BTB domains. While all four samples (two *Xl*ZBTB8A^{BTB} variants ± UBC9) crystallised in similar conditions and the same crystal form, generally producing datasets at similar resolution, the highest-resolution dataset that we used for model building was obtained using *Xl*ZBTB8A^{BTB} with the MG- extension and in the presence of UBC9. The extension sequence is not visible in the crystal structure and did not make any difference to the structure based on the comparison with lower resolution datasets lacking the extension. UBC9 is absent from the crystal.

Crystals were cryo-protected by immersion in a cryo-protective solution (pure reservoir for *Xl*ZBTB8A^{BTB} WT, S103A, and S103D; 25% v/v ethylene glycol and 75% reservoir for *Xl*ZBTB8A^{BTB} S103R; 33% *v*/*v* glycerol and 67% *v*/*v* reservoir for *Hs*ZBTB18^{BTB}). After a 5-second soak, crystals were rapidly cooled by immersing in liquid nitrogen. X-ray diffraction data were collected at 100 K on PROXIMA-1 beamline at SOLEIL synchrotron. The diffraction data were processed using XDS[105] and AIMLESS[106]. Molecular replacement with an AlphaFold2 model of a given protein as a search model was performed using Phaser [107] of the Phenix suite[108]. The atomic model was refined with phenix.refine and manually rebuilt using COOT[109]. The data collection and refinement statistics are shown in **Table 1**. The model quality was evaluated using MolProbity[110]. Prior to creating figures, missing amino-acid side-chains were added using the Protein Repair and Analysis Server (https://www.protein-science.com)[111] with standard settings except for not adding hydrogen atoms. Molecular graphics images were generated using PyMOL[112] or UCSF Chimera[113].

Crystal structure analysis

Interface analysis was performed using the PISA server[114], accessed through the PDBe platform (https://www.ebi.ac.uk/pdbe/pisa/). Structural alignments and RMSD determination over core Cα atoms were performed in PyMOL[112] using the 'super' command with 'and name ca' added to the names of the aligned objects. Sequence conservation mapping was performed using the ConSurf server[115,116] with default settings except for the range of sequence identity included in automatically generated multiple sequence alignment, which was set to 60%–95%, which we previously verified to correspond to an approximate range of sequence identity across the BTB domain between ZBTB8A proteins from fish to humans.

NALIM native MS method

MALDI-TOF MS (Matrix Assisted Laser Desorption Ionization Time of Flight Mass Spectrometry) of intact BTB oligomers was performed using an original native MS (nMS) method called NALIM (Native Liquid MALDI)[48].

Intermediate dilutions of *Xl*ZBTB8A^{BTB} WT and S103R proteins were prepared in a glycerol/water (50:50, v/v) solution containing 50 mM ammonium acetate at pH 7.5.

The matrix used for analysis is an ionic liquid matrix called HAG, composed of α-cyano-4-hydroxycinnamic acid (HCCA), 3-aminoquinoline (3AQ), and glycerol in the proportion 1:4.5:7.5 w/w. The liquid matrix was prepared as previously described [48] and samples diluted at a ratio of 1/4 in HAG. A 1 µL aliquot of this matrix-sample solution was spotted onto an MTX stainless steel sample stage (Bruker Daltonics, Germany). The droplet was left at room temperature for 15 minutes in order to evaporate residual water from the solution. The matrix-sample spot was further allowed to spend 15 minutes in the source vacuum before the acquisition, a time defined as *in vacuo* residence time (t_{ivr})[48]. *Xl*ZBTB8A^{BTB} WT and S103R mutant proteins were analysed at a final concentration of 2.5 µM by NALIM-TOF MS using a Bruker UltrafleXtreme MALDI-TOF/TOF mass spectrometer equipped with a Smartbeam II laser and PAN^{TM} technology. Spectra were acquired in linear positive ion mode using Bruker FlexControl software v.4 with a 2 730 ns delay and 20 kV acceleration voltage, accumulating 400 laser shots in a single-shot pattern. Ion deflection was applied below 10 000 Da. Spectra were processed using FlexAnalysis software v.4 (Bruker).

High-performance liquid chromatography (HPLC) size-exclusion chromatography (SEC) coupled to small-angle X-ray light scattering (SAXS)

The SAXS data were collected at the SWING beamline[117] at the SOLEIL synchrotron using an Eiger 4M detector at a distance of 2 m. During measurements, the temperature was set to 293 K. For WT and S103R *Xl*ZBTB8A^{BTB} constructs, a stock solution of each fragment was prepared at 10 mg/mL in 25 mM HEPES, pH 7.5 with 150 mM NaCl, and 0.5 mM TCEP, respectively. Protein samples (50 µl at 10 mg/ml or ~570 µM) were injected onto a BioSEC-3 300Å, 4.6 x 300 mm, 3 µm SEC column (Agilent) and eluted directly into the SAXS flow-through capillary cell at a flow rate of 0.3 ml/min. 630 SAXS frames (exposure time: 990 ms, dead time: 10 ms) were collected continuously after 6.5-min elution. 180 SAXS frames accounting for buffer scattering were collected before the column void volume. The averaged buffer scattering was then subtracted from the protein signal. SAXS curves displaying a constant radius of gyration (R_g) in an R_g versus frame number plot were averaged and were used for further characterisation. Data reduction to absolute unit was performed with FOXTROT[118]. Frame averaging and subtraction were conducted with the BioXTAS RAW software[119] as well as the $I(0)$ and R_g determination. The distance distribution function $P(r)$ and the maximum particle diameter (DMAX) were calculated using the GNOM program of the ATSAS suite[120] or BIFT in BioXTAS RAW[121]. Data were deposited in the Small Angle Scattering Biological Data Bank (SASBDB)[122].

Transmission electron microscopy (TEM)

Samples of *Xl*ZBTB8A^{BTB}, WT and S103R, were analysed with TEM using the negative staining method. 3 µl sample at 0.02 mg/ml (~1.1 µM) was deposited on a carbon-coated grid prepared using glow-discharge air plasma. The sample was blotted and rinsed with 2 % w/v uranyl acetate and dried. Microscopy was performed at 100 kV using Tecnai Spirit transmission electron microscope (ThermoFisher) equipped with a K2 Base 4k x 4k camera (Ametek/Gatan). The magnification of 34,500x (pixel size of 1.4 Å at the level of the specimen) was used for all images.

High-speed atomic force microscopy (HS-AFM)

2 µl of *Xl*ZBTB8A^{BTB} WT at 3 µM in 25 mM HEPES, pH 7.5, 150 mM NaCl, 0.5 mM TCEP was incubated on the mica surface for 10 minutes. After washing with the same buffer, the sample was immersed in the liquid cell of 100 µl of the same buffer. HS-AFM imaging was conducted using amplitude modulation mode optimised for high-resolution imaging parameters with a modified HS-AFM (SS-NEX, Research Institute of Biomolecule Metrology, Tsukuba, Japan). Short cantilevers designed for HS–AFM, equipped with an electron beam deposition (EBD) tip, were utilised (USC-F1.2-k0.15 Nanoworld, Neuchâtel, Switzerland), characterized by a nominal spring constant k = 0.15 N/m, a resonance frequency in liquid of F_0 ~ 500 kHz, and a quality factor Qc ~ 2. All experiments were conducted at room temperature. For height profile determination, N = 101 particles from a single experiment were analysed and the value presented in the text as mean ± standard deviation,

Image analysis was performed with WsXM[123] and ImageJ[124].

Phylogenetic analysis

Full-length sequences of the main isoform of each canonical human ZBTB protein were derived from UniProt[125] and aligned and organised into a phylogenetic tree using ClustalOmega[126,127] *via* the EMBL-EBI bioinformatics platform with standard settings. The tree was exported to and replotted using Interactive Tree Of Life (iTOL), version 5[128], followed by further modifications in Adobe Illustrator CS6.

BLAST analysis

Protein BLAST[51] searches using selected sequences from **Table S1** as queries were performed through the BLASTp website (https://blast.ncbi.nlm.nih.gov/Blast.cgi?PAGE=Proteins) with "*Homo sapiens*" selected as the organism and otherwise using default settings.

AlphaFold2 structural modelling

Structural modelling of the tetramers of BTB domains of human ZBTB proteins was performed using ColabFold (https://colabfold.com, version 1.5.5)[44], an on-line platform that combines multiple sequence alignment using MMseqs2[129] with structure prediction using AlphaFold2 in Multimer version 3[45,130]. Structures of tetramers were modelled by inputting four times the analysed sequence separated by colons. In addition to modelling the structures of the tetramers of the crystallised *Xl*ZBTB8A^{BTB} and *Hs*ZBTB18^{BTB} sequences, structural models of tetramers of BTB domains of each canonical human ZBTB protein were calculated. To identify regions in each protein that correspond to the BTB domain together with any potential conserved extensions, we analysed precalculated AlphaFold2 models deposited in the AlphaFold Protein Structure Database (https://AlphaFold.ebi.ac.uk)[131] and small multiple-sequence alignments of orthologues of each protein from several organisms. The analysed protein regions are listed in **Table S1**. All the predictions were performed using default settings including "mmseqs2_uniref_env multiple sequence" alignment mode and "unpaired_paired" pairing mode. The models were then analysed using PyMOL to compare the relative arrangement of the two dimers in a modelled tetramer to interdimer contacts observed in the experimental *Xl*ZBTB8A^{BTB} structure.

Live-cell imaging

U2OS WT cells were seeded into eight-well Imaging Chamber CG (Zell-Kontakt) and transfected 48 hours before imaging with plasmids indicated in figures using X-tremeGENE 360 (Sigma-Aldrich) transfection reagent according to the manufacturer's instructions. For the imaging experiments investigating the nuclear localization of the mCherry-tagged ZBTB proteins, nuclei were stained with Hoechst 33342 (333 ng/ml) for 1 hour at 37 °C prior to imaging. Immediately before imaging, growth medium was replaced with a CO_2-independent imaging medium: phenol red–free Leibovitz's L-15 medium (Life Technologies) supplemented with 20% FBS, 2 mM glutamine, penicillin (100 U/ml), and streptomycin (100 µg/ml). Live-cell imaging experiments were performed using a ZEISS LSM980 confocal laser scanning microscope with a 63x/1.4-numerical aperture (N/A) oil-immersion objective lens. Cells were kept at 37 °C using a pre-heated chamber. The fluorescence of Hoechst 33342, eGFP and mCherry was excited with lasers at 405, 488, and 561 nm, respectively. FRAP experiments were performed by bleaching a 1-µm radius circular area using 100% power of a 561-nm laser. Images were collected at the frequency of 20 frames/s. A representative image is shown.

For FRAP curves, *N* = 16 cells were examined per condition. FRAP image analysis was performed in ImageJ[124].

Luciferase reporter assay

Approximately 24 hours prior to the transfection, 4 x 10^5 COS-7 cells were seeded in 6-well plates. Cotransfection experiments were performed using 1250 ng of the BS10-pGL3-Control firefly luciferase reporter construct and 0, 25, or 100 ng of an effector vector expressing untagged ZBTB18 (WT, S102R, or K426E/R427E) in opti-MEM without phenol red. Additionally, we added 125 ng of the pRL-SV40 plasmid (Promega) containing renilla luciferase as an internal control for transfection efficiency. DNA was mixed with PLUS reagent (Thermo Fisher) in a 1:1 ratio and incubated for 15 minutes at room temperature, followed by the addition of Lipofectamine LTX (Thermo Fisher). After incubation for 25 minutes at room temperature, the growth medium was changed and each mixture was added to the well. After approximately 40 hours, the cells were harvested for the luciferase assay performed by using The Dual-Luciferase Reporter (DLR) Assay System (Promega). Transfected cells were washed once with PBS and the lysates were prepared by manually scraping the cells from the plates in the presence of 1x Passive Lysis Buffer (PLB) (Promega). The firefly and renilla luciferase activities of the extract were measured according to the manufacturer's instructions using Clariostar (BMG Labtech). Each biological replicate corresponded to a well of cultured cells, independently transfected, grown, and lysed.

Immunoblotting

Proteins from cell lysates prepared as described in the luciferase reporter assay section were concentrated with the standard TCA (trichloroacetic acid) precipitation method and separated on a 4-20% gradient Tris-glycine stain-free pre-cast gel (BioRad), followed by semi-dry electrotransfer onto a nitrocellulose membrane. Blots were developed using appropriate antibodies in 5% w/v nonfat dry milk in Tris-buffered saline with 0.1% Tween 20 detergent (TBST) buffer. Anti-ZBTB18 (Proteintech) was used at a dilutation of 1:2,000 followed by an HRP-conjugated anti-rabbit secondary antibody (Thermo Fisher) at 1:10,000. Anti-β-Actin-HRP (Santa Cruz Biotechnology) was used at 1:10,000. Membranes already blotted with anti-ZBTB18 were re-blotted with anti-β-Actin without stripping. Blots were developed by

chemiluminescence using the WesternBright ECL HRP substrate (Advansta) and IBright system (ThermoFischer).

Quantitative reverse-transcription polymerase chain reaction (RT-qPCR)

U2OS WT cells were seeded into six-well plates and transfected for 48 hours with either empty GFP, *Hs*ZBTB18-GFP WT, and *Hs*ZBTB18-GFP S102R plasmids before total RNA extraction (NucleoSpin RNA, Macherey-Nagel GmbH). RNA template was reverse-transcribed into cDNA by using the RevertAid Reverse Transcriptase (Thermo Fisher Scientific). Real-Time PCR amplification experiments were performed with the Master Mix PCR Power SYBR Green (Thermo Fisher Scientific) on a QuantStudio 7 Flex Real-Time PCR System (Thermo Fisher Scientific). The relative fold gene expression was calculated using the $2^{-\Delta\Delta CT}$ method and results were normalised to the 18S rRNA expression. The sequences of the primers used in this study are listed in **Table S2**.

Quantification and statistical analysis

SAXS data analysis

The fiber X-ray scattering pattern of a continuous helix of pitch p and radius r_0 is composed of meridian layer lines of integer index *n*. Each meridional layer line is localized at $q_z\ (n) = n \cdot q_z^0$ with $q_z^0 = 2\pi/p$ and the radial profile intensity of each line is a function of radial scattering vector q_r :

$$I_n(q_r) = I_n^{\circ} \cdot [J_n(q_r \cdot r_0)]^2$$

where J_n is the Bessel function of order *n*. The theoretical X-ray scattering is the sum of all layers normalised by the Ewald sphere surface.

$$I_{model}(q) = \left(\sum_{n=0}^{3} I_n(q_r)\right) \Big/ q^2 + A$$

With $q_r = (q^2 - (n \cdot q_z^0)^2)^{\frac{1}{2}}$ and *A* as a constant

The three former layer line profiles $\boldsymbol{I}_n(\boldsymbol{q})$ added to the central scattering (*n*=0) were fitted simultaneously by optimizing p and r_0 as well as the four I_n° and the constant, by minimising

$$\sum \left(\frac{I_{exp}(q) - I_{model}(q)}{I_{model}(q)}\right)^2$$

between *q* = 0.03 Å^{-1} and *q* = 0.26 Å^{-1} using the Solver tool of Excel.

The simulations of each layer and their sum are shown in **Figure 1I**.

The model with p = 15.3 nm and r_0 = 3.9 nm is in good agreement with the observed SAXS modulations. The variations of p are around ± 1.5 nm and those of r_0 are around ± 0.3 nm.

The parameters are given in **Table S3**.

Crystallographic data statistics

Statistics of crystallographic data collection and refinement were determined according to the standard methods in the field as explained in Method details and presented in **Table 1**.

Other methods

Quantitative data were presented as mean ± standard deviation or mean ± standard error of the mean as indicated in Method details or figure legends. Differences between samples in **Figure 7B**, represented with asterisks, were calculated using One-way ANOVA (ANalysis Of VAriance) with post-hoc Tukey HSD (Honestly Significant Difference) (https://astatsa.com/OneWay_Anova_with_TukeyHSD/).

References

1. Zollman, S., Godt, D., Privé, G.G., Couderc, J.L., and Laski, F.A. (1994). The BTB domain, found primarily in zinc finger proteins, defines an evolutionarily conserved family that includes several developmentally regulated genes in Drosophila. Proc. Natl. Acad. Sci. *91*, 10717–10721. https://doi.org/10.1073/pnas.91.22.10717.

2. Siggs, O., and Beutler, B. (2012). The BTB-ZF transcription factors. Cell Cycle *11*, 3358–3369. https://doi.org/10.4161/cc.21277.

3. Kelly, K.F., and Daniel, J.M. (2006). POZ for effect--POZ-ZF transcription factors in cancer and development. Trends Cell Biol. *16*, 578–587. https://doi.org/10.1016/j.tcb.2006.09.003.

4. Cheng, Z.-Y., He, T.-T., Gao, X.-M., Zhao, Y., and Wang, J. (2021). ZBTB Transcription Factors: Key Regulators of the Development, Differentiation and Effector Function of T Cells. Front. Immunol. *12*.

5. Lee, S.-U., and Maeda, T. (2012). POK/ZBTB proteins: an emerging family of proteins that regulate lymphoid development and function: POK/ZBTB protein in lymphoid development. Immunol. Rev. *247*, 107–119. https://doi.org/10.1111/j.1600-065X.2012.01116.x.

6. Maeda, T. (2016). Regulation of hematopoietic development by ZBTB transcription factors. Int. J. Hematol. *104*, 310–323. https://doi.org/10.1007/s12185-016-2035-x.

7. McLachlan, T., Matthews, W.C., Jackson, E.R., Staudt, D.E., Douglas, A.M., Findlay, I.J., Persson, M.L., Duchatel, R.J., Mannan, A., Germon, Z.P., et al. (2022). B-cell Lymphoma 6 (BCL6): From Master Regulator of Humoral Immunity to Oncogenic Driver in Pediatric Cancers. Mol. Cancer Res. MCR *20*, 1711–1723. https://doi.org/10.1158/1541-7786.MCR-22-0567.

8. Kim, M.-K., Jeon, B.-N., Koh, D.-I., Kim, K.-S., Park, S.-Y., Yun, C.-O., and Hur, M.-W. (2013). Regulation of the cyclin-dependent kinase inhibitor 1A gene (CDKN1A) by the repressor BOZF1 through inhibition of p53 acetylation and transcription factor Sp1 binding. J. Biol. Chem. *288*, 7053–7064. https://doi.org/10.1074/jbc.M112.416297.

9. Aoki, K., Meng, G., Suzuki, K., Takashi, T., Kameoka, Y., Nakahara, K., Ishida, R., and Kasai, M. (1998). RP58 Associates with Condensed Chromatin and Mediates a Sequence-specific Transcriptional Repression *. J. Biol. Chem. *273*, 26698–26704. https://doi.org/10.1074/jbc.273.41.26698.

10. Xiang, C., Baubet, V., Pal, S., Holderbaum, L., Tatard, V., Jiang, P., Davuluri, R.V., and Dahmane, N. (2012). RP58/ZNF238 directly modulates proneurogenic gene levels and is required for neuronal differentiation and brain expansion. Cell Death Differ. *19*, 692–702. https://doi.org/10.1038/cdd.2011.144.

11. Ohtaka-Maruyama, C., Hirai, S., Miwa, A., Heng, J.I.-T., Shitara, H., Ishii, R., Taya, C., Kawano, H., Kasai, M., Nakajima, K., et al. (2013). RP58 Regulates the Multipolar-Bipolar Transition of Newborn Neurons in the Developing Cerebral Cortex. Cell Rep. *3*, 458–471. https://doi.org/10.1016/j.celrep.2013.01.012.

12. Xiang, C., Frietze, K.K., Bi, Y., Li, Y., Dal Pozzo, V., Pal, S., Alexander, N., Baubet, V., D'Acunto, V., Mason, C.E., et al. (2021). RP58 Represses Transcriptional Programs Linked to Nonneuronal Cell Identity and Glioblastoma Subtypes in Developing Neurons. Mol. Cell. Biol. *41*, e00526-20. https://doi.org/10.1128/MCB.00526-20.

13. Hirai, S., Miwa, H., Shimbo, H., Nakajima, K., Kondo, M., Tanaka, T., Ohtaka-Maruyama, C., Hirai, S., and Okado, H. (2023). The mouse model of intellectual disability by ZBTB18/RP58 haploinsufficiency shows

cognitive dysfunction with synaptic impairment. Mol. Psychiatry, 1–12. https://doi.org/10.1038/s41380-023-01941-3.

14. Lu, C., Garipler, G., Dai, C., Roush, T., Salome-Correa, J., Martin, A., Liscovitch-Brauer, N., Mazzoni, E.O., and Sanjana, N.E. (2023). Essential transcription factors for induced neuron differentiation. Nat. Commun. *14*, 8362. https://doi.org/10.1038/s41467-023-43602-7.

15. de Munnik, S.A., García-Miñaúr, S., Hoischen, A., van Bon, B.W., Boycott, K.M., Schoots, J., Hoefsloot, L.H., Knoers, N.V., Bongers, E.M., and Brunner, H.G. (2014). A de novo non-sense mutation in ZBTB18 in a patient with features of the 1q43q44 microdeletion syndrome. Eur. J. Hum. Genet. *22*, 844–846. https://doi.org/10.1038/ejhg.2013.249.

16. Cohen, J.S., Srivastava, S., Farwell Hagman, K.D., Shinde, D.N., Huether, R., Darcy, D., Wallerstein, R., Houge, G., Berland, S., Monaghan, K.G., et al. (2017). Further evidence that de novo missense and truncating variants in ZBTB18 cause intellectual disability with variable features. Clin. Genet. *91*, 697–707. https://doi.org/10.1111/cge.12861.

17. van der Schoot, V., de Munnik, S., Venselaar, H., Elting, M., Mancini, G.M.S., Ravenswaaij-Arts, C.M.A., Anderlid, B., Brunner, H.G., and Stevens, S.J.C. (2018). Toward clinical and molecular understanding of pathogenic variants in the ZBTB18 gene. Mol. Genet. Genomic Med. *6*, 393–400. https://doi.org/10.1002/mgg3.387.

18. Hemming, I.A., Clément, O., Gladwyn-Ng, I.E., Cullen, H.D., Ng, H.L., See, H.B., Ngo, L., Ulgiati, D., Pfleger, K.D.G., Agostino, M., et al. (2019). Disease-associated missense variants in ZBTB18 disrupt DNA binding and impair the development of neurons within the embryonic cerebral cortex. Hum. Mutat. *40*, 1841–1855. https://doi.org/10.1002/humu.23803.

19. Fedele, V., Dai, F., Masilamani, A.P., Heiland, D.H., Kling, E., Gätjens-Sanchez, A.M., Ferrarese, R., Platania, L., Doostkam, S., Kim, H., et al. (2017). Epigenetic Regulation of ZBTB18 Promotes Glioblastoma Progression. Mol. Cancer Res. *15*, 998–1011. https://doi.org/10.1158/1541-7786.MCR-16-0494.

20. Bazzocco, S., Dopeso, H., Martínez-Barriocanal, Á., Anguita, E., Nieto, R., Li, J., García-Vidal, E., Maggio, V., Rodrigues, P., de Marcondes, P.G., et al. (2021). Identification of ZBTB18 as a novel colorectal tumor suppressor gene through genome-wide promoter hypermethylation analysis. Clin. Epigenetics *13*, 88. https://doi.org/10.1186/s13148-021-01070-0.

21. Ferrarese, R., Izzo, A., Andrieux, G., Lagies, S., Bartmuss, J.P., Masilamani, A.P., Wasilenko, A., Osti, D., Faletti, S., Schulzki, R., et al. (2023). ZBTB18 inhibits SREBP-dependent lipid synthesis by halting CTBPs and LSD1 activity in glioblastoma. Life Sci. Alliance *6*. https://doi.org/10.26508/lsa.202201400.

22. Wang, R., Bhatt, A.B., Minden-Birkenmaier, B.A., Travis, O.K., Tiwari, S., Jia, H., Rosikiewicz, W., Martinot, O., Childs, E., Loesch, R., et al. (2023). ZBTB18 restricts chromatin accessibility and prevents transcriptional adaptations that drive metastasis. Sci. Adv. *9*, eabq3951. https://doi.org/10.1126/sciadv.abq3951.

23. Bardwell, V.J., and Treisman, R. (1994). The POZ domain: a conserved protein-protein interaction motif. Genes Dev. *8*, 1664–1677. https://doi.org/10.1101/gad.8.14.1664.

24. Stogios, P.J., Downs, G.S., Jauhal, J.J., Nandra, S.K., and Privé, G.G. (2005). Sequence and structural analysis of BTB domain proteins. Genome Biol. *6*, R82. https://doi.org/10.1186/gb-2005-6-10-r82.

25. Bonchuk, A., Balagurov, K., and Georgiev, P. (2022). BTB domains: A structural view of evolution, multimerization, and protein–protein interactions. BioEssays, 2200179. https://doi.org/10.1002/bies.202200179.

26. Ahmad, K.F., Melnick, A., Lax, S., Bouchard, D., Liu, J., Kiang, C.-L., Mayer, S., Takahashi, S., Licht, J.D., and Privé, G.G. (2003). Mechanism of SMRT Corepressor Recruitment by the BCL6 BTB Domain. Mol. Cell *12*, 1551–1564. https://doi.org/10.1016/S1097-2765(03)00454-4.

27. Ghetu, A.F., Corcoran, C.M., Cerchietti, L., Bardwell, V.J., Melnick, A., and Privé, G.G. (2008). Structure of a BCOR corepressor peptide in complex with the BCL6 BTB domain dimer. Mol. Cell *29*, 384–391. https://doi.org/10.1016/j.molcel.2007.12.026.

28. Kang, S.I., Chang, W.-J., Cho, S.-G., and Kim, I.Y. (2003). Modification of Promyelocytic Leukemia Zinc Finger Protein (PLZF) by SUMO-1 Conjugation Regulates Its Transcriptional Repressor Activity *. J. Biol. Chem. *278*, 51479–51483. https://doi.org/10.1074/jbc.M309237200.

29. Chao, T.-T., Chang, C.-C., and Shih, H.-M. (2007). SUMO modification modulates the transrepression activity of PLZF. Biochem. Biophys. Res. Commun. *358*, 475–482. https://doi.org/10.1016/j.bbrc.2007.04.157.

30. Matic, I., Schimmel, J., Hendriks, I.A., Santen, M.A. van, Rijke, F. van de, Dam, H. van, Gnad, F., Mann, M., and Vertegaal, A.C.O. (2010). Site-Specific Identification of SUMO-2 Targets in Cells Reveals an Inverted SUMOylation Motif and a Hydrophobic Cluster SUMOylation Motif. Mol. Cell *39*, 641–652. https://doi.org/10.1016/j.molcel.2010.07.026.

31. DelRosso, N., Tycko, J., Suzuki, P., Andrews, C., Aradhana, Mukund, A., Liongson, I., Ludwig, C., Spees, K., Fordyce, P., et al. (2023). Large-scale mapping and mutagenesis of human transcriptional effector domains. Nature *616*, 365–372. https://doi.org/10.1038/s41586-023-05906-y.

32. Lobanova, Y., Filonova, G., Kaplun, D., Zhigalova, N., Prokhortchouk, E., and Zhenilo, S. (2023). TRIM28 regulates transcriptional activity of methyl-DNA binding protein Kaiso by SUMOylation. Biochimie *206*, 73–80. https://doi.org/10.1016/j.biochi.2022.10.006.

33. Fang, Z., Deng, Y., Wang, H., and Zhou, J. (2024). SUMOylation of zebrafish transcription factor Zbtb21 affects its transcription activity. PeerJ *12*, e17234. https://doi.org/10.7717/peerj.17234.

34. Bonchuk, A.N., Balagurov, K.I., Baradaran, R., Boyko, K.M., Sluchanko, N.N., Khrustaleva, A.M., Burtseva, A.D., Arkova, O.V., Khalisova, K.K., Popov, V.O., et al. (2024). The Arthropoda-specific Tramtrack group BTB protein domains use previously unknown interface to form hexamers. Preprint at bioRxiv, https://doi.org/10.1101/2022.09.01.506177 https://doi.org/10.1101/2022.09.01.506177.

35. Espinás, M.L., Jiménez-García, E., Vaquero, A., Canudas, S., Bernués, J., and Azorín, F. (1999). The N-terminal POZ Domain of GAGA Mediates the Formation of Oligomers That Bind DNA with High Affinity and Specificity *. J. Biol. Chem. *274*, 16461–16469. https://doi.org/10.1074/jbc.274.23.16461.

36. Katsani, K.R., Hajibagheri, M.A.N., and Verrijzer, C.P. (1999). Co-operative DNA binding by GAGA transcription factor requires the conserved BTB/POZ domain and reorganizes promoter topology. EMBO J. *18*, 698–708. https://doi.org/10.1093/emboj/18.3.698.

37. Tang, X., Li, T., Liu, S., Wisniewski, J., Zheng, Q., Rong, Y., Lavis, L.D., and Wu, C. (2022). Kinetic principles underlying pioneer function of GAGA transcription factor in live cells. Nat. Struct. Mol. Biol. *29*, 665–676. https://doi.org/10.1038/s41594-022-00800-z.

38. Stead, M.A., Trinh, C.H., Garnett, J.A., Carr, S.B., Baron, A.J., Edwards, T.A., and Wright, S.C. (2007). A Beta-Sheet Interaction Interface Directs the Tetramerisation of the Miz-1 POZ Domain. J. Mol. Biol. *373*, 820–826. https://doi.org/10.1016/j.jmb.2007.08.026.

39. Ahmad, K.F., Engel, C.K., and Privé, G.G. (1998). Crystal structure of the BTB domain from PLZF. Proc. Natl. Acad. Sci. *95*, 12123–12128. https://doi.org/10.1073/pnas.95.21.12123.

40. Li, X., Peng, H., Schultz, D.C., Lopez-Guisa, J.M., Rauscher, F.J., III, and Marmorstein, R. (1999). Structure-Function Studies of the BTB/POZ Transcriptional Repression Domain from the Promyelocytic Leukemia Zinc Finger Oncoprotein1. Cancer Res. *59*, 5275–5282.

41. Schubot, F.D., Tropea, J.E., and Waugh, D.S. (2006). Structure of the POZ domain of human LRF, a master regulator of oncogenesis. Biochem. Biophys. Res. Commun. *351*, 1–6. https://doi.org/10.1016/j.bbrc.2006.09.167.

42. Bienz, M. (2020). Head-to-Tail Polymerization in the Assembly of Biomolecular Condensates. Cell *182*, 799–811. https://doi.org/10.1016/j.cell.2020.07.037.

43. Fiedler, M., Franco-Echevarría, E., Schulten, A., Nielsen, M., Rutherford, T.J., Yeates, A., Ahsan, B., Dean, C., and Bienz, M. (2022). Head-to-tail polymerization by VEL proteins underpins cold-induced Polycomb silencing in flowering control. Cell Rep. *41*, 111607. https://doi.org/10.1016/j.celrep.2022.111607.

44. Mirdita, M., Schütze, K., Moriwaki, Y., Heo, L., Ovchinnikov, S., and Steinegger, M. (2022). ColabFold: making protein folding accessible to all. Nat. Methods *19*, 679–682. https://doi.org/10.1038/s41592-022-01488-1.

45. Jumper, J., Evans, R., Pritzel, A., Green, T., Figurnov, M., Ronneberger, O., Tunyasuvunakool, K., Bates, R., Žídek, A., Potapenko, A., et al. (2021). Highly accurate protein structure prediction with AlphaFold. Nature *596*, 583–589. https://doi.org/10.1038/s41586-021-03819-2.

46. Evans, R., O'Neill, M., Pritzel, A., Antropova, N., Senior, A., Green, T., Žídek, A., Bates, R., Blackwell, S., and Yim, J. (2022). Protein complex prediction with AlphaFold-Multimer. BioRxiv, 2021–10.

47. Malkov, S.N., Zivković, M.V., Beljanski, M.V., Hall, M.B., and Zarić, S.D. (2008). A reexamination of the propensities of amino acids towards a particular secondary structure: classification of amino acids based on their chemical structure. J. Mol. Model. *14*, 769–775. https://doi.org/10.1007/s00894-008-0313-0.

48. Beaufour, M., Ginguené, D., Le Meur, R., Castaing, B., and Cadene, M. (2018). Liquid Native MALDI Mass Spectrometry for the Detection of Protein-Protein Complexes. J. Am. Soc. Mass Spectrom. *29*, 1981–1994. https://doi.org/10.1007/s13361-018-2015-x.

49. Li, X., Lopez-Guisa, J.M., Ninan, N., Weiner, E.J., Rauscher, F.J., and Marmorstein, R. (1997). Overexpression, Purification, Characterization, and Crystallization of the BTB/POZ Domain from the PLZF Oncoprotein *. J. Biol. Chem. *272*, 27324–27329. https://doi.org/10.1074/jbc.272.43.27324.

50. Piepoli, S., Barakat, S., Nogay, L., Şimşek, B., Akkose, U., Taskiran, H., Tolay, N., Gezen, M., Yeşilada, C.Y., Tuncay, M., et al. (2022). Sibling rivalry among the ZBTB transcription factor family: homodimers versus heterodimers. Life Sci. Alliance *5*. https://doi.org/10.26508/lsa.202201474.

51. Altschul, S.F., Gish, W., Miller, W., Myers, E.W., and Lipman, D.J. (1990). Basic local alignment search tool. J. Mol. Biol. *215*, 403–410. https://doi.org/10.1016/S0022-2836(05)80360-2.

52. Stead, M.A., Carr, S.B., and Wright, S.C. (2009). Structure of the human Nac1 POZ domain. Acta Crystallograph. Sect. F Struct. Biol. Cryst. Commun. *65*, 445–449. https://doi.org/10.1107/S1744309109012214.

53. Schwarz-Romond, T., Merrifield, C., Nichols, B.J., and Bienz, M. (2005). The Wnt signalling effector Dishevelled forms dynamic protein assemblies rather than stable associations with cytoplasmic vesicles. J. Cell Sci. *118*, 5269–5277. https://doi.org/10.1242/jcs.02646.

54. Schwarz-Romond, T., Fiedler, M., Shibata, N., Butler, P.J.G., Kikuchi, A., Higuchi, Y., and Bienz, M. (2007). The DIX domain of Dishevelled confers Wnt signaling by dynamic polymerization. Nat. Struct. Mol. Biol. *14*, 484–492. https://doi.org/10.1038/nsmb1247.

55. Marzahn, M.R., Marada, S., Lee, J., Nourse, A., Kenrick, S., Zhao, H., Ben-Nissan, G., Kolaitis, R., Peters, J.L., Pounds, S., et al. (2016). Higher-order oligomerization promotes localization of SPOP to liquid nuclear speckles. EMBO J. *35*, 1254–1275. https://doi.org/10.15252/embj.201593169.

56. Thul, P.J., Åkesson, L., Wiking, M., Mahdessian, D., Geladaki, A., Ait Blal, H., Alm, T., Asplund, A., Björk, L., Breckels, L.M., et al. (2017). A subcellular map of the human proteome. Science *356*, eaal3321. https://doi.org/10.1126/science.aal3321.

57. Reynolds, R.C., Montgomery, P.O., and Hughes, B. (1964). Nucleolar “Caps” Produced by Actinomycin D*. Cancer Res. *24*, 1269–1277.

58. Bizhanova, A., and Kaufman, P.D. (2021). Close to the edge: Heterochromatin at the nucleolar and nuclear peripheries. Biochim. Biophys. Acta BBA - Gene Regul. Mech. *1864*, 194666. https://doi.org/10.1016/j.bbagrm.2020.194666.

59. Bersaglieri, C., Kresoja-Rakic, J., Gupta, S., Bär, D., Kuzyakiv, R., Panatta, M., and Santoro, R. (2022). Genome-wide maps of nucleolus interactions reveal distinct layers of repressive chromatin domains. Nat. Commun. *13*, 1483. https://doi.org/10.1038/s41467-022-29146-2.

60. Lallemand-Breitenbach, V., and Thé, H. de (2010). PML Nuclear Bodies. Cold Spring Harb. Perspect. Biol. *2*, a000661. https://doi.org/10.1101/cshperspect.a000661.

61. Hemming, I.A., Blake, S., Agostino, M., and Heng, J.I.-T. (2020). General population ZBTB18 missense variants influence DNA binding and transcriptional regulation. Hum. Mutat. *41*, 1629–1644. https://doi.org/10.1002/humu.24069.

62. Wang, S., Xu, Z., Li, M., Lv, M., Shen, S., Shi, Y., and Li, F. (2023). Structural insights into the recognition of telomeric variant repeat TTGGGG by Krüppel-like C2H2 finger protein ZBTB10. J. Biol. Chem. *0*. https://doi.org/10.1016/j.jbc.2023.102918.

63. Masilamani, A.P., Schulzki, R., Yuan, S., Haase, I.V., Kling, E., Dewes, F., Andrieux, G., Börries, M., Schnell, O., Heiland, D.H., et al. (2022). Calpain-mediated cleavage generates a ZBTB18 N-terminal product that regulates HIF1A signaling and glioblastoma metabolism. iScience *25*, 104625. https://doi.org/10.1016/j.isci.2022.104625.

64. Słabicki, M., Yoon, H., Koeppel, J., Nitsch, L., Roy Burman, S.S., Di Genua, C., Donovan, K.A., Sperling, A.S., Hunkeler, M., Tsai, J.M., et al. (2020). Small-molecule-induced polymerization triggers degradation of BCL6. Nature *588*, 164–168. https://doi.org/10.1038/s41586-020-2925-1.

65. Feng, W., Wu, H., Chan, L.-N., and Zhang, M. (2007). The Par-3 NTD adopts a PB1-like structure required for Par-3 oligomerization and membrane localization. EMBO J. *26*, 2786–2796. https://doi.org/10.1038/sj.emboj.7601702.

66. Bienz, M. (2014). Signalosome assembly by domains undergoing dynamic head-to-tail polymerization. Trends Biochem. Sci. *39*, 487–495. https://doi.org/10.1016/j.tibs.2014.08.006.

67. van Dop, M., Fiedler, M., Mutte, S., de Keijzer, J., Olijslager, L., Albrecht, C., Liao, C.-Y., Janson, M.E., Bienz, M., and Weijers, D. (2020). DIX Domain Polymerization Drives Assembly of Plant Cell Polarity Complexes. Cell *180*, 427-439.e12. https://doi.org/10.1016/j.cell.2020.01.011.

68. Riccio, A.A., McCauley, M., Langelier, M.-F., and Pascal, J.M. (2016). Tankyrase sterile α motif domain polymerization is required for its role in Wnt signaling. Structure *24*, 1573–1581.

69. Mariotti, L., Templeton, C.M., Ranes, M., Paracuellos, P., Cronin, N., Beuron, F., Morris, E., and Guettler, S. (2016). Tankyrase requires SAM domain-dependent polymerization to support Wnt-β-catenin signaling. Mol. Cell *63*, 498–513.

70. Pillay, N., Mariotti, L., Zaleska, M., Inian, O., Jessop, M., Hibbs, S., Desfosses, A., Hopkins, P.C.R., Templeton, C.M., Beuron, F., et al. (2022). Structural basis of tankyrase activation by polymerization. Nature *612*, 162–169. https://doi.org/10.1038/s41586-022-05449-8.

71. Cuneo, M.J., O'Flynn, B.G., Lo, Y.-H., Sabri, N., and Mittag, T. (2023). Higher-order SPOP assembly reveals a basis for cancer mutant dysregulation. Mol. Cell *83*, 731-745.e4. https://doi.org/10.1016/j.molcel.2022.12.033.

72. Kim, C.A., Gingery, M., Pilpa, R.M., and Bowie, J.U. (2002). The SAM domain of polyhomeotic forms a helical polymer. Nat. Struct. Biol. *9*, 453–457. https://doi.org/10.1038/nsb802.

73. Isono, K., Endo, T.A., Ku, M., Yamada, D., Suzuki, R., Sharif, J., Ishikura, T., Toyoda, T., Bernstein, B.E., and Koseki, H. (2013). SAM Domain Polymerization Links Subnuclear Clustering of PRC1 to Gene Silencing. Dev. Cell *26*, 565–577. https://doi.org/10.1016/j.devcel.2013.08.016.

74. Afroz, T., Hock, E.-M., Ernst, P., Foglieni, C., Jambeau, M., Gilhespy, L.A.B., Laferriere, F., Maniecka, Z., Plückthun, A., Mittl, P., et al. (2017). Functional and dynamic polymerization of the ALS-linked protein TDP-43 antagonizes its pathologic aggregation. Nat. Commun. *8*, 45. https://doi.org/10.1038/s41467-017-00062-0.

75. Wang, A., Conicella, A.E., Schmidt, H.B., Martin, E.W., Rhoads, S.N., Reeb, A.N., Nourse, A., Ramirez Montero, D., Ryan, V.H., Rohatgi, R., et al. (2018). A single N-terminal phosphomimic disrupts TDP-43 polymerization, phase separation, and RNA splicing. EMBO J. *37*, e97452. https://doi.org/10.15252/embj.201797452.

76. Kim, C.A., Phillips, M.L., Kim, W., Gingery, M., Tran, H.H., Robinson, M.A., Faham, S., and Bowie, J.U. (2001). Polymerization of the SAM domain of TEL in leukemogenesis and transcriptional repression. EMBO J. *20*, 4173–4182. https://doi.org/10.1093/emboj/20.15.4173.

77. Qiao, F., Song, H., Kim, C.A., Sawaya, M.R., Hunter, J.B., Gingery, M., Rebay, I., Courey, A.J., and Bowie, J.U. (2004). Derepression by Depolymerization: Structural Insights into the Regulation of Yan by Mae. Cell *118*, 163–173. https://doi.org/10.1016/j.cell.2004.07.010.

78. Knight, M.J., Leettola, C., Gingery, M., Li, H., and Bowie, J.U. (2011). A human sterile alpha motif domain polymerizome. Protein Sci. *20*, 1697–1706. https://doi.org/10.1002/pro.703.

79. Korasick, D.A., Westfall, C.S., Lee, S.G., Nanao, M.H., Dumas, R., Hagen, G., Guilfoyle, T.J., Jez, J.M., and Strader, L.C. (2014). Molecular basis for AUXIN RESPONSE FACTOR protein interaction and the control of auxin response repression. Proc. Natl. Acad. Sci. *111*, 5427–5432. https://doi.org/10.1073/pnas.1400074111.

80. Sayou, C., Nanao, M.H., Jamin, M., Posé, D., Thévenon, E., Grégoire, L., Tichtinsky, G., Denay, G., Ott, F., Peirats Llobet, M., et al. (2016). A SAM oligomerization domain shapes the genomic binding landscape of the LEAFY transcription factor. Nat. Commun. *7*, 11222. https://doi.org/10.1038/ncomms11222.

81. Powers, S.K., Holehouse, A.S., Korasick, D.A., Schreiber, K.H., Clark, N.M., Jing, H., Emenecker, R., Han, S., Tycksen, E., Hwang, I., et al. (2019). Nucleo-cytoplasmic Partitioning of ARF Proteins Controls Auxin Responses in Arabidopsis thaliana. Mol. Cell *76*, 177-190.e5. https://doi.org/10.1016/j.molcel.2019.06.044.

82. Bertolini, M., Fenzl, K., Kats, I., Wruck, F., Tippmann, F., Schmitt, J., Auburger, J.J., Tans, S., Bukau, B., and Kramer, G. (2021). Interactions between nascent proteins translated by adjacent ribosomes drive homomer assembly. Science *371*, 57–64. https://doi.org/10.1126/science.abc7151.

83. Mallik, S., Venezian, J., Lobov, A., Heidenreich, M., Garcia-Seisdedos, H., Yeates, T.O., Shiber, A., and Levy, E.D. (2024). Structural determinants of co-translational protein complex assembly. Preprint at bioRxiv, https://doi.org/10.1101/2024.01.20.576408 https://doi.org/10.1101/2024.01.20.576408.

84. Melnick, A., Ahmad, K.F., Arai, S., Polinger, A., Ball, H., Borden, K.L., Carlile, G.W., Prive, G.G., and Licht, J.D. (2000). In-depth mutational analysis of the promyelocytic leukemia zinc finger BTB/POZ domain reveals motifs and residues required for biological and transcriptional functions. Mol. Cell. Biol. *20*, 6550–6567. https://doi.org/10.1128/MCB.20.17.6550-6567.2000.

85. Thomasen, F.E., Cuneo, M.J., Mittag, T., and Lindorff-Larsen, K. (2023). Conformational and oligomeric states of SPOP from small-angle X-ray scattering and molecular dynamics simulations. eLife *12*, e84147. https://doi.org/10.7554/eLife.84147.

86. Thanos, C.D., Goodwill, K.E., and Bowie, J.U. (1999). Oligomeric Structure of the Human EphB2 Receptor SAM Domain. Science *283*, 833–836. https://doi.org/10.1126/science.283.5403.833.

87. Lukatsky, D.B., Shakhnovich, B.E., Mintseris, J., and Shakhnovich, E.I. (2007). Structural similarity enhances interaction propensity of proteins. J. Mol. Biol. *365*, 1596–1606. https://doi.org/10.1016/j.jmb.2006.11.020.

88. Schulz, G.E. (2010). The Dominance of Symmetry in the Evolution of Homo-oligomeric Proteins. J. Mol. Biol. *395*, 834–843. https://doi.org/10.1016/j.jmb.2009.10.044.

89. Garcia-Seisdedos, H., Empereur-Mot, C., Elad, N., and Levy, E.D. (2017). Proteins evolve on the edge of supramolecular self-assembly. Nature *548*, 244–247. https://doi.org/10.1038/nature23320.

90. Schweke, H., Levin, T., Pacesa, M., Goverde, C.A., Kumar, P., Duhoo, Y., Dornfeld, L.J., Dubreuil, B., Georgeon, S., Ovchinnikov, S., et al. (2023). An atlas of protein homo-oligomerization across domains of life. Preprint at bioRxiv, https://doi.org/10.1101/2023.06.09.544317 https://doi.org/10.1101/2023.06.09.544317.

91. Green, S.M., Coyne, H.J., McIntosh, L.P., and Graves, B.J. (2010). DNA binding by the ETS protein TEL (ETV6) is regulated by autoinhibition and self-association. J. Biol. Chem. *285*, 18496–18504. https://doi.org/10.1074/jbc.M109.096958.

92. Hope, C.M., Rebay, I., and Reinitz, J. (2017). DNA Occupancy of Polymerizing Transcription Factors: A Chemical Model of the ETS Family Factor Yan. Biophys. J. *112*, 180–192. https://doi.org/10.1016/j.bpj.2016.11.901.

93. Hope, C.M., Webber, J.L., Tokamov, S.A., and Rebay, I. (2018). Tuned polymerization of the transcription factor Yan limits off-DNA sequestration to confer context-specific repression. eLife *7*, e37545. https://doi.org/10.7554/eLife.37545.

94. Johnson, A.D., Meyer, B.J., and Ptashne, M. (1979). Interactions between DNA-bound repressors govern regulation by the λ phage repressor. Proc. Natl. Acad. Sci. *76*, 5061–5065. https://doi.org/10.1073/pnas.76.10.5061.

95. Hochschild, A., and Ptashne, M. (1986). Cooperative binding of lambda repressors to sites separated by integral turns of the DNA helix. Cell *44*, 681–687. https://doi.org/10.1016/0092-8674(86)90833-0.

96. Webber, J.L., Zhang, J., Cote, L., Vivekanand, P., Ni, X., Zhou, J., Nègre, N., Carthew, R.W., White, K.P., and Rebay, I. (2013). The Relationship Between Long-Range Chromatin Occupancy and Polymerization of the Drosophila ETS Family Transcriptional Repressor Yan. Genetics *193*, 633–649. https://doi.org/10.1534/genetics.112.146647.

97. Webber, J.L., and Rebay, I. (2013). Chromatin occupancy patterns of the ETS repressor Yan: A mechanism for buffering gene expression against noise? Fly (Austin) *7*, 92–98. https://doi.org/10.4161/fly.24162.

98. Zhang, J., Graham, T.G.W., Vivekanand, P., Cote, L., Cetera, M., and Rebay, I. (2010). Sterile Alpha Motif Domain-Mediated Self-Association Plays an Essential Role in Modulating the Activity of the Drosophila ETS Family Transcriptional Repressor Yan. Mol. Cell. Biol. *30*, 1158–1170. https://doi.org/10.1128/MCB.01225-09.

99. Britton, H.M., Levine, A.B., Shen, Y., Mungall, K., Serrano, J., Snuderl, M., Pleasance, E., Jones, S.J.M., Laskin, J., Marra, M.A., et al. (2021). NTRK2 Fusion driven pediatric glioblastoma: Identification of oncogenic Drivers via integrative Genome and transcriptome profiling. Clin. Case Rep. *9*, 1472–1477. https://doi.org/10.1002/ccr3.3804.

100. Levine, Shen, Y., Mungall, K., Serrano, J., Snuderl, M., Pleasance, E., Jones, S.J.M., Laskin, J., Marra, M.A., Rassekh, R., et al. (2019). NTRK2 Fusion Driven Pediatric Glioblastoma: Identification of key molecular drivers by personalized oncology. Can. J. Neurol. Sci. *46*, S64–S64. https://doi.org/10.1017/cjn.2019.266.

101. Zanazzi, G., Pendrick, D., Lin, C.-C., Higgins, D., Bruce, J.A., Roth, K.A., and Hsiao, S. (2020). Pineal Region High-Grade Glioneuronal Tumor With a Novel ZBTB10-NTRK3 Fusion. J. Neuropathol. Exp. Neurol. *79*, 929–931. https://doi.org/10.1093/jnen/nlaa065.

102. Nitsch, L., Jensen, P., Yoon, H., Koeppel, J., Burman, S.S.R., Fischer, E.S., Scholl, C., Fröhling, S., and Słabicki, M. (2022). BTBBCL6 dimers as building blocks for reversible drug-induced protein oligomerization. Cell Rep. Methods *2*, 100193. https://doi.org/10.1016/j.crmeth.2022.100193.

103. Tognon, C.E., Mackereth, C.D., Somasiri, A.M., McIntosh, L.P., and Sorensen, P.H.B. (2004). Mutations in the SAM domain of the ETV6-NTRK3 chimeric tyrosine kinase block polymerization and transformation activity. Mol. Cell. Biol. *24*, 4636–4650. https://doi.org/10.1128/MCB.24.11.4636-4650.2004.

104. Goffinont, S., Coste, F., Prieu-Serandon, P., Mance, L., Gaudon, V., Garnier, N., Castaing, B., and Suskiewicz, M.J. (2023). Structural insights into the regulation of the human E2∼SUMO conjugate through analysis of its stable mimetic. J. Biol. Chem. *299*. https://doi.org/10.1016/j.jbc.2023.104870.

105. Kabsch, W. (2010). XDS. Acta Crystallogr. D Biol. Crystallogr. *66*, 125–132. https://doi.org/10.1107/S0907444909047337.

106. Evans, P.R., and Murshudov, G.N. (2013). How good are my data and what is the resolution? Acta Crystallogr. D Biol. Crystallogr. *69*, 1204–1214. https://doi.org/10.1107/S0907444913000061.

107. McCoy, A.J. (2007). Solving structures of protein complexes by molecular replacement with Phaser. Acta Crystallogr. D Biol. Crystallogr. *63*, 32–41. https://doi.org/10.1107/S0907444906045975.

108. Adams, P.D., Afonine, P.V., Bunkóczi, G., Chen, V.B., Davis, I.W., Echols, N., Headd, J.J., Hung, L.-W., Kapral, G.J., Grosse-Kunstleve, R.W., et al. (2010). PHENIX: a comprehensive Python-based system for macromolecular structure solution. Acta Crystallogr. D Biol. Crystallogr. *66*, 213–221. https://doi.org/10.1107/S0907444909052925.

109. Emsley, P., and Cowtan, K. (2004). Coot: model-building tools for molecular graphics. Acta Crystallogr. D Biol. Crystallogr. *60*, 2126–2132. https://doi.org/10.1107/S0907444904019158.

110. Davis, I.W., Leaver-Fay, A., Chen, V.B., Block, J.N., Kapral, G.J., Wang, X., Murray, L.W., Arendall, W.B., Snoeyink, J., Richardson, J.S., et al. (2007). MolProbity: all-atom contacts and structure validation for proteins and nucleic acids. Nucleic Acids Res. *35*, W375-383. https://doi.org/10.1093/nar/gkm216.

111. Nnyigide, O.S., Nnyigide, T.O., Lee, S.-G., and Hyun, K. (2022). Protein Repair and Analysis Server: A Web Server to Repair PDB Structures, Add Missing Heavy Atoms and Hydrogen Atoms, and Assign Secondary Structures by Amide Interactions. J. Chem. Inf. Model. *62*, 4232–4246. https://doi.org/10.1021/acs.jcim.2c00571.

112. Schrödinger, L., and DeLano, W. (2020). PyMOL.

113. Pettersen, E.F., Goddard, T.D., Huang, C.C., Couch, G.S., Greenblatt, D.M., Meng, E.C., and Ferrin, T.E. (2004). UCSF Chimera—A visualization system for exploratory research and analysis. J. Comput. Chem. *25*, 1605–1612. https://doi.org/10.1002/jcc.20084.

114. Krissinel, E., and Henrick, K. (2007). Inference of Macromolecular Assemblies from Crystalline State. J. Mol. Biol. *372*, 774–797. https://doi.org/10.1016/j.jmb.2007.05.022.

115. Glaser, F., Pupko, T., Paz, I., Bell, R.E., Bechor-Shental, D., Martz, E., and Ben-Tal, N. (2003). ConSurf: identification of functional regions in proteins by surface-mapping of phylogenetic information. Bioinforma. Oxf. Engl. *19*, 163–164. https://doi.org/10.1093/bioinformatics/19.1.163.

116. Yariv, B., Yariv, E., Kessel, A., Masrati, G., Chorin, A.B., Martz, E., Mayrose, I., Pupko, T., and Ben-Tal, N. (2023). Using evolutionary data to make sense of macromolecules with a “face-lifted” ConSurf. Protein Sci. Publ. Protein Soc. *32*, e4582. https://doi.org/10.1002/pro.4582.

117. Thureau, A., Roblin, P., and Pérez, J. (2021). BioSAXS on the SWING beamline at Synchrotron SOLEIL. J. Appl. Crystallogr. *54*, 1698–1710. https://doi.org/10.1107/S1600576721008736.

118. Girardot, R., Viguier, G., Pérez, J., and Ounsy, M. (2015). FOXTROT: A JAVA-based application to reduce and analyse SAXS and WAXS piles of 2D data at synchrotron SOLEIL. In Proceedings of the 8th canSAS Meeting, Tokai, Japan, pp. 14–16.

119. Hopkins, J.B., Gillilan, R.E., and Skou, S. (2017). BioXTAS RAW: improvements to a free open-source program for small-angle X-ray scattering data reduction and analysis. J. Appl. Crystallogr. *50*, 1545–1553. https://doi.org/10.1107/S1600576717011438.

120. Manalastas-Cantos, K., Konarev, P.V., Hajizadeh, N.R., Kikhney, A.G., Petoukhov, M.V., Molodenskiy, D.S., Panjkovich, A., Mertens, H.D.T., Gruzinov, A., Borges, C., et al. (2021). ATSAS 3.0: expanded functionality and new tools for small-angle scattering data analysis. J. Appl. Crystallogr. *54*, 343–355. https://doi.org/10.1107/S1600576720013412.

121. Hansen, S. (2000). Bayesian estimation of hyperparameters for indirect Fourier transformation in small-angle scattering. J. Appl. Crystallogr. *33*, 1415–1421. https://doi.org/10.1107/S0021889800012930.

122. Valentini, E., Kikhney, A.G., Previtali, G., Jeffries, C.M., and Svergun, D.I. (2015). SASBDB, a repository for biological small-angle scattering data. Nucleic Acids Res. *43*, D357–D363. https://doi.org/10.1093/nar/gku1047.

123. Horcas, I., Fernández, R., Gómez-Rodríguez, J.M., Colchero, J., Gómez-Herrero, J., and Baro, A.M. (2007). WSXM: a software for scanning probe microscopy and a tool for nanotechnology. Rev. Sci. Instrum. *78*, 013705. https://doi.org/10.1063/1.2432410.

124. Schneider, C.A., Rasband, W.S., and Eliceiri, K.W. (2012). NIH Image to ImageJ: 25 years of image analysis. Nat. Methods *9*, 671–675. https://doi.org/10.1038/nmeth.2089.

125. The UniProt Consortium (2023). UniProt: the Universal Protein Knowledgebase in 2023. Nucleic Acids Res. *51*, D523–D531. https://doi.org/10.1093/nar/gkac1052.

126. Sievers, F., Wilm, A., Dineen, D., Gibson, T.J., Karplus, K., Li, W., Lopez, R., McWilliam, H., Remmert, M., Söding, J., et al. (2011). Fast, scalable generation of high-quality protein multiple sequence alignments using Clustal Omega. Mol. Syst. Biol. *7*, 539. https://doi.org/10.1038/msb.2011.75.

127. Goujon, M., McWilliam, H., Li, W., Valentin, F., Squizzato, S., Paern, J., and Lopez, R. (2010). A new bioinformatics analysis tools framework at EMBL–EBI. Nucleic Acids Res. *38*, W695–W699. https://doi.org/10.1093/nar/gkq313.

128. Letunic, I., and Bork, P. (2021). Interactive Tree Of Life (iTOL) v5: an online tool for phylogenetic tree display and annotation. Nucleic Acids Res. *49*, W293–W296. https://doi.org/10.1093/nar/gkab301.

129. Steinegger, M., and Söding, J. (2017). MMseqs2 enables sensitive protein sequence searching for the analysis of massive data sets. Nat. Biotechnol. *35*, 1026–1028. https://doi.org/10.1038/nbt.3988.

130. Evans, R., O'Neill, M., Pritzel, A., Antropova, N., Senior, A., Green, T., Žídek, A., Bates, R., Blackwell, S., Yim, J., et al. (2022). Protein complex prediction with AlphaFold-Multimer. Preprint at bioRxiv, https://doi.org/10.1101/2021.10.04.463034 https://doi.org/10.1101/2021.10.04.463034.

131. Varadi, M., Anyango, S., Deshpande, M., Nair, S., Natassia, C., Yordanova, G., Yuan, D., Stroe, O., Wood, G., and Laydon, A. (2022). AlphaFold Protein Structure Database: massively expanding the structural coverage of protein-sequence space with high-accuracy models. Nucleic Acids Res. *50*, D439–D444.